

Novel photoelectrocatalytic system of oxygen vacancy-rich black TiO_{2-x} nanocones photoanode and natural air diffusion cathode for efficient water purification and simultaneous H₂O₂ production

Ruiheng Liang ^{a,b}, Huizhong Wu ^{a,b}, Zhongzheng Hu ^{a,b}, Jiangli Sun ^{a,b}, Chunhong Fu ^{a,b}, Shuaishuai Li ^{a,b}, Xiuwu Zhang ^{a,b}, Minghua Zhou ^{a,b,*}

^a Tianjin Key Laboratory of Environmental Technology for Complex Trans-Media Pollution, College of Environmental Science and Engineering, Nankai University, Tianjin 300350, China

^b Key Laboratory of Pollution Process and Environmental Criteria, Ministry of Education, College of Environmental Science and Engineering, Nankai University, Tianjin 300350, China



ARTICLE INFO

Keywords:

Photoelectrocatalytic system
Water purification
H₂O₂ production
Synergistic effect
Oxygen vacancy

ABSTRACT

Photoelectrocatalytic (PEC) system harnesses solar energy for chemical reactions, representing a highly promising renewable energy-based technology for water purification. Herein, we design a novel separated PEC system that integrates water purification on an oxygen vacancy-rich black TiO₂ nanocones (b-TiO_{2-x}) photoanode with two-electron O₂ reduction reaction for H₂O₂ production on a natural air diffusion cathode. This integration benefits from thermodynamic advantages, synergy effects and enhanced •OH production, thus exhibiting superior water purification (98.32%, 0.064 min⁻¹) and H₂O₂ production (6.83 μmol/h/cm²) at ultra-low applied cell voltage of 0.5 V, with the energy consumption of only 0.034 kWh/m³ wastewater treated, where the simultaneous production of value-added H₂O₂ could fully compensate for the electric cost of the system. Notably, even under real sunlight irradiation, this system achieves efficient water purification and H₂O₂ production without additional energy consumption, offering a cost-effective and environmental-benign strategy for the dual purpose of water purification and resourcization.

1. Introduction

Access to safe, sufficient, and affordable water is vital to well-being and to the economy [1]. Unfortunately, water pollution has become an increasingly serious challenge due to emerging organic contaminants, such as antibiotics, phenolic compounds, and dyes [2]. These contaminants may be removed by traditional wastewater treatment systems combining physical, chemical, and biological processes [3,4]. However, conventional methods are generally energy-intensive, suffering from high energy consumption, where clean and renewable sources will be better choices, i.e., solar energy [5]. Solar power, enabling its energy to meet the yearly energy demand of the world within merely 1 h, can assist in addressing energy crisis, if it can be fully utilized [6]. Hence, the development and application of solar energy for water purification is one of the most necessary and urgent topics.

The emerging solar energy-driven photoelectrocatalytic (PEC) system

synergizes the advantages of electrocatalytic (EC) and photocatalytic (PC) system, suppressing photogenerated electron-hole pairs recombination with an external bias potential [7,8]. PEC system has potential for coupling both oxidative and reductive half-reactions in a single photoelectroreduox catalytic cycle, where both photogenerated electrons and holes can drive useful redox reactions [6,9]. In this way, this dual-functional PEC system can make full use of the potential energy stored in both photogenerated carriers, being essential for achieving solar economy [9]. However, current PEC systems face dilemma, which is commonly attributed to the following three critical factors. First, a high applied bias voltage (1.0–2.0 V vs. Ag/AgCl) for efficient degradation of organic pollutants is necessary, resulting in high energy consumption. Second, there is insufficient research on the targeted utilization of photogenerated electrons at the cathode of PEC system, further leading to the neglect of the synergistic interaction between the cathode and photoanode. Third, the photoanode of PEC system has poor

* Corresponding author at: Tianjin Key Laboratory of Environmental Technology for Complex Trans-Media Pollution, College of Environmental Science and Engineering, Nankai University, Tianjin 300350, China.

E-mail address: zhoumh@nankai.edu.cn (M. Zhou).

performance of generating hydroxyl radical ($\cdot\text{OH}$), hindering efficient pollutant removal. Thus, energy consumption, resourcization, and removal efficiency of organic pollutants will be the focal points to build highly efficient PEC processes.

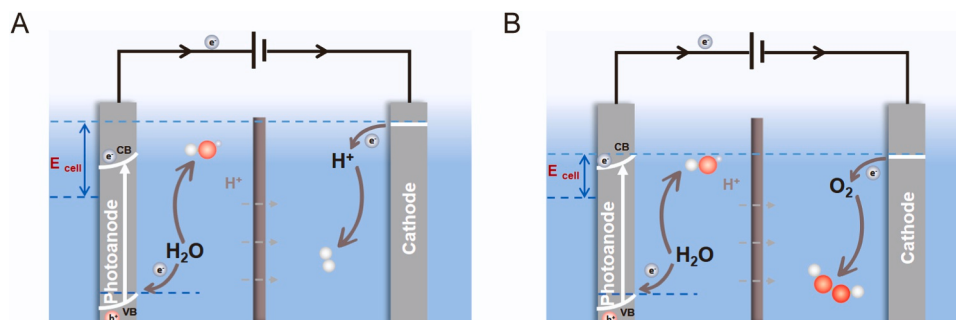
To date, many researchers have developed anodic oxidation reactions as an alternative one to oxygen evolution reaction (OER), such as oxidizing small molecule alcohols and aldehydes [10,11], monomeric sugar molecules [12] and urea [13,14], which can greatly lower the voltage input, together with integrating cathodic H_2 production or H_2O_2 electrosynthesis. Regrettably, from the perspective of wastewater treatment, the aforementioned alternative anodic reactions are not suitable for application, because the photoanode in PEC wastewater treatment system is expected to produce hydroxyl radicals ($\cdot\text{OH}$) for pollutant removal via water oxidation, which is also more favorable and valuable than OER process. Based on this, we originally propose a novel cathode substitution strategy aimed at lowering voltage input. Notably, the two-electron oxygen reduction reaction (2e⁻ORR) process ($\text{O}_2 + 2 \text{H}^+ + 2\text{e}^- \rightarrow \text{H}_2\text{O}_2$, 0.68 V vs. RHE) is thermodynamically favored compared to hydrogen evolution reaction (HER) process ($2 \text{H}^+ + 2\text{e}^- \rightarrow \text{H}_2$, 0 V vs. RHE) due to its more positive equilibrium potential [15,16], in which the system needs lower voltage to drive the removal of pollution and can produce H_2O_2 simultaneously (Scheme 1). Thus, our PEC system will utilize this thermodynamically favorable reaction to reduce the total energy input and maximize profitability by producing value-added H_2O_2 at the cathode.

Meanwhile, the present photoanode for pollutant removal is mainly coupled with Pt cathode as a counter electrode, where the targeted utilization of photogenerated electron is often ignored, commonly attributed to two factors. First, the efficiency of degrading pollutants is mainly determined by the performance of photoanode rather than cathode. Second, H_2 produced in cathode within the cathodic HER is difficult to collect and store, leading to inferior economic value. Considering the above two factors, we aim to make full use of the photogenerated electron induced from photoanode to reduce O_2 to value-added H_2O_2 at cathode, by which the synergistic effect between photoanode and cathode will be further revealed. In this way, the novel integration is anticipated to solve the dilemmas of energy consumption and resourcization in current PEC processes.

In term of pollutant removal efficiency, it is directly determined by the generation of hole and $\cdot\text{OH}$ in PEC system for water purification, as the pollutants are usually removed by holes (direct oxidation) and $\cdot\text{OH}$ from water oxidation (indirect oxidation) [17]. In order to improve the production of hole and $\cdot\text{OH}$, the choice of photoanode is crucial. To date, TiO_2 has been widely used for PEC water purification, which thanks to its low toxicity, excellent stability, and more importantly, its highly positive potential of the valence band edge for generating $\cdot\text{OH}$ [18]. Nevertheless, the application of TiO_2 in PEC water purification is still limited by large band gap, low electrical conductivity and rapid recombination of photogenerated carriers [19]. In that front, much effort has been expended to improve the photoelectrochemical performance of TiO_2 such as elemental doping [20], heterojunction

construction [21,22], cocatalyst deposition [23,24], and defect engineering [25–27]. Among them, defective engineering, especially oxygen vacancy, has been proved to have a significant impact on the optical, physical and catalytic properties of materials [27–30]. Oxygen vacancy can narrow the band gap to broaden the optical response, improve the carrier concentration, as well as increase the intrinsic conductivity and carrier separation efficiency, while preserving the intrinsic TiO_2 crystal structure [27–30]. Meanwhile, oxygen vacancy shows strengths in modulating coordination structure, creating adsorption site and generating free radical. For example, Mao et al. reported that oxygen vacancies, as the capture center for electrons, provide coordinatively unsaturated sites to induce strong interactions with O_2 , delivering electrons to the chemisorbed O_2 , which achieves rapid O_2 activation to $\cdot\text{O}_2$ [31]. Furthermore, Zhan et al. elaborated that oxygen vacancies are responsible for the capture and reduction of H_2O_2 to generate $\cdot\text{OH}$ [32]. Hence, with oxygen vacancies, not only can the PEC properties of the photoelectrode itself be improved, but also the adsorption and activation of molecules are modulated, which is beneficial for producing free radicals on the surface of the photoanode, and thus constructing a PEC process with higher pollutant removal efficiency. Notably, electrochemical reduction provides simple, safe and controllable method for introducing oxygen vacancy. During electrochemical reduction, Ti^{4+} species can be reducing to Ti^{3+} at cathode ($\text{Ti}^{4+} + \text{e}^- \rightarrow \text{Ti}^{3+}$), simultaneously inducing oxygen vacancies to maintain electrostatic balance ($\text{Ti}^{4+}\text{-O-Ti}^{4+} \rightarrow \text{Ti}^{3+}\text{-Ov-Ti}^{3+}$), and the amount of oxygen vacancy can be accurately controlled by adjusting the current of electrochemical reduction [33,34].

Based on the above analysis, a dual-function PEC system can be constructed to achieve PEC water purification in the anode compartment and H_2O_2 production in the cathode compartment with lower voltage. To this end, we innovatively adopt oxygen vacancy-rich black TiO_2 nanocones photoelectrocatalyst ($b\text{-TiO}_{2-x}$) as photoanode and natural air diffusion electrode (NADE) as carbon black/PTFE cathode. On the one hand, $b\text{-TiO}_{2-x}$ is employed because oxygen vacancies over TiO_2 can significantly improve the photoelectrochemical properties, such as light absorption, as well as charge separation and transfer. These vacancies can also facilitate the adsorption of H_2O molecule and lower the energy barrier of H_2O molecule activation (transforming H_2O to $\cdot\text{OH}$). On the other hand, the NADE with a superhydrophobic three-phase interface enables molecular oxygen in the air to naturally diffuse into the reaction interface, where the energy consumption of aeration is unnecessary [35]. Herein, in this work, to address the challenges of requiring a high external applied bias voltage, the lack of targeted utilization of photogenerated electrons and the synergy of photoanode and cathode, as well as the poor performance of photoanode in generating free radicals, we report a PEC method for water purification with novel integration of $b\text{-TiO}_{2-x}$ nanocones photoanode and NADE cathode, while proving the thermodynamic advantages for driving the system with low voltage, the synergistic effect between the photoanode and the cathode, the introduction of oxygen vacancies for enhanced $\cdot\text{OH}$ production, and the applicability of this system under real sunlight,



Scheme 1. Comparison of the reaction mechanism for (A) conventional PEC-HER water purification and (B) PEC-2e⁻ORR water purification and H_2O_2 production.

which will pave the way for high-efficiency and low-consumption water purification coupled with cathodic H₂O₂ production.

2. Experimental

2.1. Preparation b-TiO_{2-x} photoanode and NADE cathode

The TiO₂ nanocones photoanode was prepared by one-step hydrothermal method [17]. Titanium isopropoxide (TTIP) was dissolved in acetylacetone (ACAC) to obtain the ACAC chelated Ti precursor. Then, Ti precursor was added into Na₂EDTA aqueous solution to assist in forming the conical structures, resulting well-oriented TiO₂ nanocone array. The Ti precursor prepared in the absence of ACAC resulted in TiO₂ nanorod arrays. The TiO₂ nanocones photoanode exhibited better PEC performance than TiO₂ nanorods photoanode due to efficient photo-generated carriers separation and mass transfer (Fig. S1). The b-TiO_{2-x} nanocones photoanode was fabricated by a combined hydrothermal approach and electrochemical reduction process. Among all the samples, the b-TiO_{2-x} photoanode with current density of 7.77 mA cm⁻² showed the best PEC performance and therefore it was chosen as the model photoanode (Fig. S2). The preparation of the NADE is according to our previous work [35]. PTFE modified carbon felt (CF) was used as gas diffusion layer and support layer, and PTFE/CB mixture was used as catalyst layer. The details for preparing the photoanode and carbon cathode were displayed in [supporting information](#).

2.2. Characterization

X-ray powder diffraction (XRD) patterns were conducted to characterize the photoanode crystal structure using Philips- 12045B/3 diffractometer equipped with Cu K α radiation source. X-ray photoelectron spectra (XPS) were performed for analyzing the surface chemical states of photoanode on a Thermo Scientific ESCALAB 250X using Al K X-rays as the excitation source. Scanning electron microscope (SEM) images were measured by a Zeiss LEO-1530VP. Transmission electron microscopy (TEM) images were obtained to observe the photoanode morphology by utilizing the JEM-2100 f. UV-vis diffuse reflectance spectrum of photoanode was recorded on a Shimadzu 2600 UV spectrophotometer. Oxygen vacancy was recorded on an electron paramagnetic resonance (EPR) spectrometer (Bruker). Photoluminescence (PL) spectra were obtained at ambient temperature using a HITACHI F-2710 fluorescence spectrophotometer. Contact angle measurements were performed to analyze the hydrophobicity property of photoanode and cathode on a goniometer (JC2000D1, POWERREACH).

2.3. Photoelectrochemical measurements

PEC measurements of TiO₂ and b-TiO_{2-x} photoanodes were conducted using the typical three-electrode configuration with photoanode as the working electrode, Pt as the counter electrode, and Ag/AgCl as the reference electrode. All measurements were conducted on an electrochemical workstation (CHI 760E, CH Instruments) using a 50 W LED lamp (100 mW cm⁻²) as light source. 0.1 M Na₂SO₄ aqueous solution was used as electrolyte for PEC measurements. Photocurrent-time (*J-t*) curves were obtained at 1 V vs Ag/AgCl with or without illumination. Linear sweep voltammetry (LSV) curves were recorded at a potential range from 0 to 1.5 V vs. Ag/AgCl at a scan rate of 10 mV s⁻¹. The electrochemical impedance spectroscopy (EIS) analyses were recorded at 1 V vs. Ag/AgCl over the frequency range from 10⁵ to 10⁻² Hz with or without illumination, and the amplitude was set at 5 mV. Mott-Schottky analysis was acquired at 1000 Hz frequency without illumination. The cyclic voltammetry (CV) curves were tested in a potential range from 0.25 to 0.35 V vs. Ag/AgCl at scan rates from 0.02 to 0.1 V s⁻¹, and the double-layer capacitance (C_{dl}) was calculated from the obtained CV curves according to the anodic–cathodic current density differences plotted against scan rates of photoanode to estimate the electrochemical

active surface area (ESCA).

The PEC system for water purification and synergistic H₂O₂ production were performed in a two-compartment reactor with the cation exchange membrane CEM-8040 (Huamo-tech). In this two-compartment reactor, the anodic compartment contained 0.1 M Na₂SO₄ in the absence or presence of 10 mg L⁻¹ sulfamethazine (SMT) solution, and the cathodic compartment contained 0.1 M Na₂SO₄. When the tests were conducted in a three-electrode system, carbon cathode or Pt cathode, photoanode and Ag/AgCl electrode served as the counter, working and reference electrode respectively. When the experiment was conducted in a two-electrode system, the counter electrode and the reference electrodes were joined together. *J-t* curves were obtained at 0.5 V with or without illumination. LSV curves were recorded at a cell voltage within the range of 0–2 V at a scan rate of 10 mV s⁻¹.

2.4. Experimental setup

The established PEC system for simultaneous water purification and H₂O₂ production was achieved in a two-compartment reactor with a quartz window and a cation exchange membrane as the division (Fig. S3 and Fig. S4). For the b-TiO_{2-x}/NADE PEC system, anodic b-TiO_{2-x} and cathodic NADE served as working and counter electrodes, respectively. For the b-TiO_{2-x}/Pt PEC system, anodic b-TiO_{2-x} and cathodic Pt were chose as working and counter electrodes, respectively. In this two-compartment reactor, 60 mL of 0.1 M Na₂SO₄ solution containing 10 mg L⁻¹ SMT was injected into anodic compartment, and the cathodic compartment contained 60 mL 0.1 M Na₂SO₄. Subsequently, the PEC reaction in this PEC system was driven by the illumination of LED light and the application of a cell voltage.

2.5. Analytical methods

The concentrations of SMT and other pollutants were analyzed by a high-performance liquid chromatography (HPLC, Thermo Fisher Scientific, U3000) using a 120 C18 column with a DAD detector at 30°C. The mobile phase and other detailed analytical parameters were shown in [Table S1](#). The removal of pollutants followed the pseudo-first-order kinetic fitting model (Eq. 1).

$$\ln(C_0/C_t) = kt \quad (1)$$

where C_0 is the initial pollutant concentration (mg L⁻¹), C_t is the pollutant concentration at time t (mg L⁻¹) and k is the pseudo first-order rate constant (min⁻¹). The H₂O₂ concentration was determined by potassium titanium oxalate (K₂TiO(C₂O₄)₂·H₂O) and spectrophotometric analysis at a maximum response wavelength of 400 nm [36]. The current efficiency (CE, %) for H₂O₂ generation was calculated according to Eq. (2).

$$CE = \frac{2CVF}{Q} \quad (2)$$

where C is the concentration of H₂O₂ (mol L⁻¹), V is the volume of reaction solution (L), F is the Faraday constant (C mol⁻¹), and Q is the amount of charge passed through the cathode (C). Total organic carbon (TOC) was detected through TOC analyzer (Shimadzu, Japan). The EPR data was recorded on a Bruker EMX Nano (Germany) using the spin-trap reagent 5,5-dimethyl-1-pyrroline N-oxide (DMPO) in H₂O for ·OH and 2,2,6,6-Tetramethyl-1-piperidinyloxy (TEMPO) in water for hole. The ·OH concentration was quantified using dimethyl sulfoxide (DMSO, 0.2%) to trap ·OH to form quantitative formaldehyde, which would react with 2,4-dinitrophenylhydrazine (DNPH) to form hydrazine (HCHO-DNPH) at phosphate buffer solution [37]. The formed hydrazine could be measured by HPLC with a DAD at 355 nm, using a mobile phase of methanol: water (60:40, v/v) at the flow rate of 0.5 mL min⁻¹.

2.6. DFT calculation

Density functional theory (DFT) calculations were adopted to compare the catalytic performance of TiO_2 to that of b- TiO_{2-x} . All DFT calculations were achieved on the Vienna ab initio simulation package (VASP 5.4.1) with the generalized gradient approximation (GGA) using the Perdew-Burke-Ernzerhof (PBE) formulation [38–40]. The cut-off energy was set as 400 eV and the k-point mesh was set as $3 \times 1 \times 1$ in Brillouin zone. The adsorption energy (E_{ads}) was calculated as Eq. (3)

$$E_{\text{ads}} = E_{\text{ad/sub}} - E_{\text{ad}} - E_{\text{sub}} \quad (3)$$

where $E_{\text{ad/sub}}$, E_{ad} and E_{sub} are the total energy of the optimized adsorbate/substrate system, the energy of isolated adsorbate, and the energy of clean substrate, respectively. The free energy (ΔG) for elemental reaction step was calculated as Eq. (4)

$$\Delta G = \Delta E + \Delta E_{\text{ZPE}} - T\Delta S \quad (4)$$

where ΔE is the difference of total energy, ΔE_{ZPE} and ΔS are the zero point energy difference and the change of entropy, respectively, T is the temperature (298.15 K in this work).

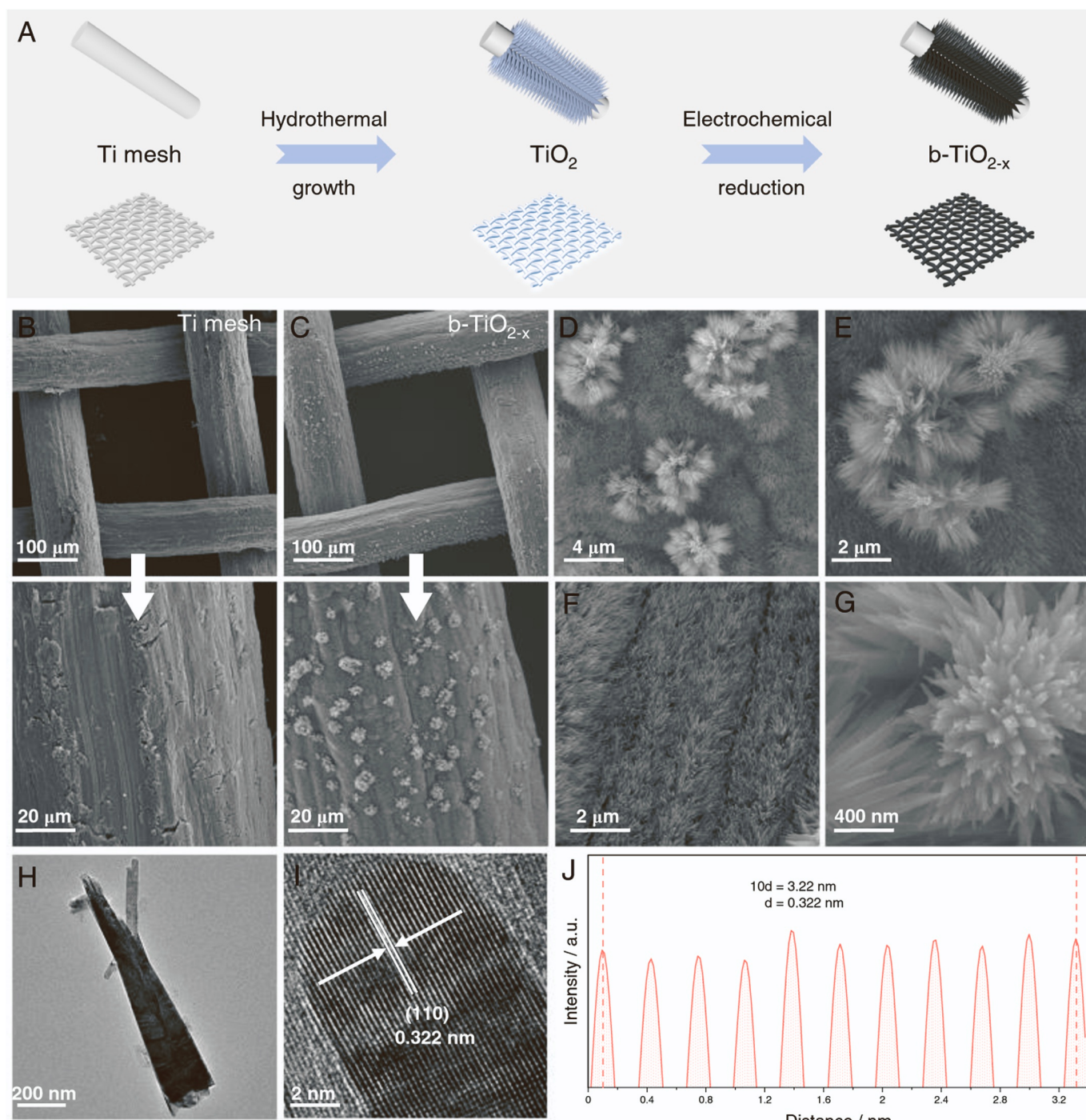


Fig. 1. (A) Schematic illustration for the synthesis of the b- TiO_{2-x} nanocones photoanode. SEM images of (B) Ti mesh and (C) Ti mesh/b- TiO_{2-x} . (D-G) SEM images of b- TiO_{2-x} . (H) TEM image and (I) HRTEM image of b- TiO_{2-x} . (G) The atomic column intensity change of b- TiO_{2-x} .

3. Results and discussion

3.1. Structural characterization

To begin with, the b-TiO_{2-x} nanocones photoanode was synthesized via a combined hydrothermal approach and electrochemical reduction process (Fig. 1A). Detailed surface morphologies of the photoanodes were observed by SEM (Fig. 1B), showing the texture structure of Ti mesh, woven by Ti wire with a diameter of about 100 μm. Network structure of Ti mesh served as the substrate, greatly improving the specific surface area and mass transfer in aqueous solution [41]. Compared to bare Ti mesh, the SEM image of b-TiO_{2-x} photoanode indicated that the nanocones were in-situ grown uniformly on the Ti mesh substrate, and even formed 3D branch-like structure with sufficient reactive areas (Fig. 1C) [17]. Further observation suggested that the diameter of these 3D branches was about 4–5 μm, and the length of nanocones was about 1 μm (Fig. 1D–G). Meanwhile, there were no noticeable morphological changes other than the change of color to black after the electrochemical reduction process (Fig. S5). The TEM showed that the diameter of the individual nanocone was about 1 μm (Fig. 1H), which was consistent with the SEM results. High-resolution TEM (HRTEM) confirmed the crystal structure of b-TiO_{2-x} with lattice spacing of 0.322 nm, closely matching the d-spacing of rutile TiO₂ in (110) plane, which indicated the axial direction of b-TiO_{2-x} and TiO₂ nanocones is along the [001] direction (Fig. 1I and J).

As shown from the XRD characterization in Fig. 2A, both b-TiO_{2-x} and TiO₂ exhibited identical rutile peaks of TiO₂ (JCPDS No. 21–1276) with (110), (101), (111) and (211) lattice plane at 27.4°, 36.1°, 41.2° and 54.3°, respectively, indicating that the electrochemical reduction treatment did not induce any phase transition in b-TiO_{2-x}. To verify the induce of oxygen vacancies in b-TiO_{2-x} through electrochemical reduction treatment, EPR spectra were employed (Fig. 2B). The b-TiO_{2-x} exhibited a remarkably stronger EPR signals at g = 2.003 owing to the free electrons trapped in oxygen vacancies (Fig. 2B) [42]. XPS were

performed to confirm the influences of reduction treatment on chemical states (Fig. 2C and D). The high-resolution O 1 s spectra displayed two main binding energy peaks at 531.7 and 529.8 eV due to the lattice oxygen and deficient oxygen respectively (Fig. 2C) [25]. Notably, the characteristic peak of deficient oxygen in b-TiO_{2-x} was obviously stronger than that in TiO₂, further indicating the successful induce of oxygen vacancies in b-TiO_{2-x} through electrochemical reduction treatment (Fig. 2C). Compared to TiO₂, the high-resolution Ti 2p spectra of b-TiO_{2-x} exhibited a slight shift toward lower binding energy, accompanied by the emergence of low-valent state Ti species (Ti³⁺) (Fig. 2D). The peaks at 463.9 and 458.4 eV were attributed to Ti³⁺ states with the abundance of 40.7%, while the peaks at 458.8 and 464.7 eV could be assigned to Ti⁴⁺ with the abundance of 59.3% (Fig. 2D). The presence of Ti³⁺ states also suggested the formation of oxygen vacancies that maintain the electrostatic balance [43]. Considering the above EPR results, the XPS results fully testified the introduction of oxygen vacancies in b-TiO_{2-x}.

The UV-vis absorption spectra of the pristine TiO₂ and b-TiO_{2-x} were exhibited in Fig. 2E. Compared to the pristine TiO₂, the b-TiO_{2-x} photoanode presented a red shift of the spectrum with dramatically enhanced absorption in visible region, manifesting the electrochromism to black. Meanwhile, the bandgap energy (E_g) of photoanodes could be calculated via the Eq. (5) [44].

$$\alpha h\nu = A (h\nu - E_g)^2 \quad (5)$$

where α represents absorption coefficient, $h\nu$ represents photonic energy, A represents proportionality constant, and E_g represents bandgap energy. The b-TiO_{2-x} exhibited a narrower bandgap (2.93 eV) than that of TiO₂ (3.01 eV) (Fig. 2F). This shortened bandgap is generally attributed to that oxygen vacancy results in the upward shift of Fermi level and introduce defect energy levels within the bandgap, which has been reported in many metal oxide semiconductor systems, such as TiO₂, ZnO and SnO₂ [34,45,46]. Furthermore, ultraviolet photoemission spectroscopy (UPS) can accurately determine the energy from vacuum to the

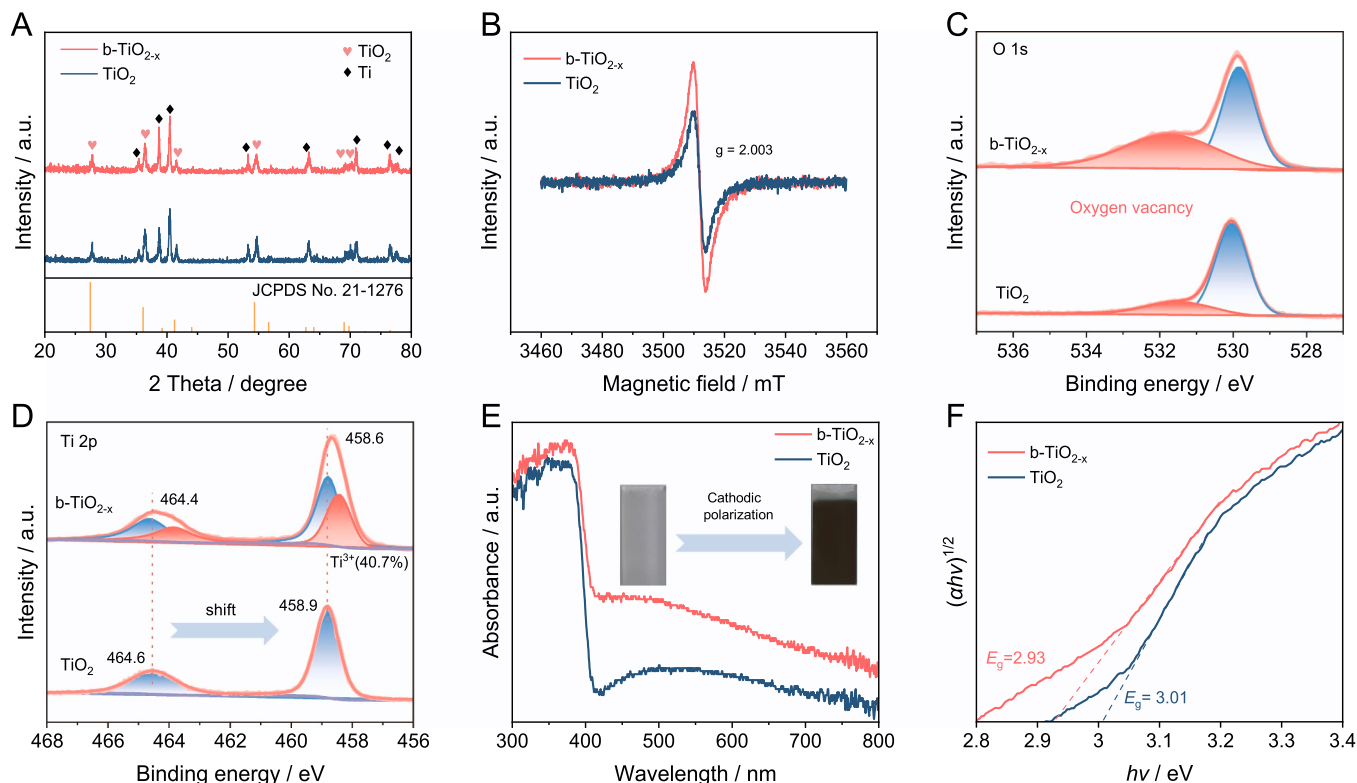


Fig. 2. (A) XRD patterns and (B) EPR spectra of b-TiO_{2-x} and TiO₂. XPS spectra for (C) the O 1 s regions and (D) the Ti 2p regions of b-TiO_{2-x} and TiO₂. (E) UV-vis DRS spectra (insert is the variation of apparent color) and (F) corresponding Tauc plots of b-TiO_{2-x} and TiO₂.

Fermi level (work function) and the energy from the Fermi level to the valence band maximum to determine the valence band position (E_V) and Fermi level (E_F) of semiconductors [24]. As shown in Fig. S6, the work function of TiO_2 and b-TiO_{2-x} were 4.83 eV and 4.69 eV, respectively, and the valence band maximum of the TiO_2 and b-TiO_{2-x} were 2.75 eV and 2.48 eV, respectively. Thus, the E_V of TiO_2 and b-TiO_{2-x} were -7.58 and -7.17 eV vs. vacuum or 3.14 and 2.73 eV on the NHE scale. Based on these two E_V values and the equation $E_C = E_V - E_g$ [24], the conduction band position (E_C) of TiO_2 and b-TiO_{2-x} were further calculated to be 0.13 and -0.2 V vs. RHE. Herein, the intrinsic band structures of the TiO_2 and b-TiO_{2-x} were obtained in Fig. S6C.

3.2. Energy-saving water purification enabled by integration of b-TiO_{2-x} photoanode and NADE cathode

The activities of b-TiO_{2-x} /NADE PEC system and traditional PEC system ($\text{b-TiO}_{2-x}/\text{Pt}$) were compared in terms of the degradation

performance of SMT removal. Only about 70.53% SMT could be degraded by the traditional PEC system (Fig. 3A). Notably, the SMT degradation efficiency of the b-TiO_{2-x} /NADE PEC system reached to 98.32% with the reaction rate constant (k -value) of 0.064 min^{-1} , which was nearly 3.2 times of that in traditional PEC system (0.02 min^{-1}) (Fig. 3A). Meanwhile, the H_2O_2 production in b-TiO_{2-x} /NADE PEC system reached to 34.8 mg/L , while that in traditional PEC system could be negligible (Fig. 3B). Notably, when b-TiO_{2-x} /NADE PEC system was operated in the single-compartment reactor, H_2O_2 formed at the cathode tended to be easily degraded at the photoanode, which lowered the overall H_2O_2 production to 4.73 mg L^{-1} , comparing to its production of 34.82 mg L^{-1} in the dual-compartment reactor (Fig. S4A). Meanwhile, the PEC degeneration performance of b-TiO_{2-x} also significantly decreased (Fig. S4B). It is attributed to the fact that H_2O_2 , as the hole scavenger, readily reacts with holes to form oxygen and water ($2 \text{ H}_2\text{O}_2 + h^+ \rightarrow \text{O}_2 + 2 \text{ H}_2\text{O}$), thus further hindering the pollutant removal efficiency. These results indicated that this novel integration of b-TiO_{2-x}

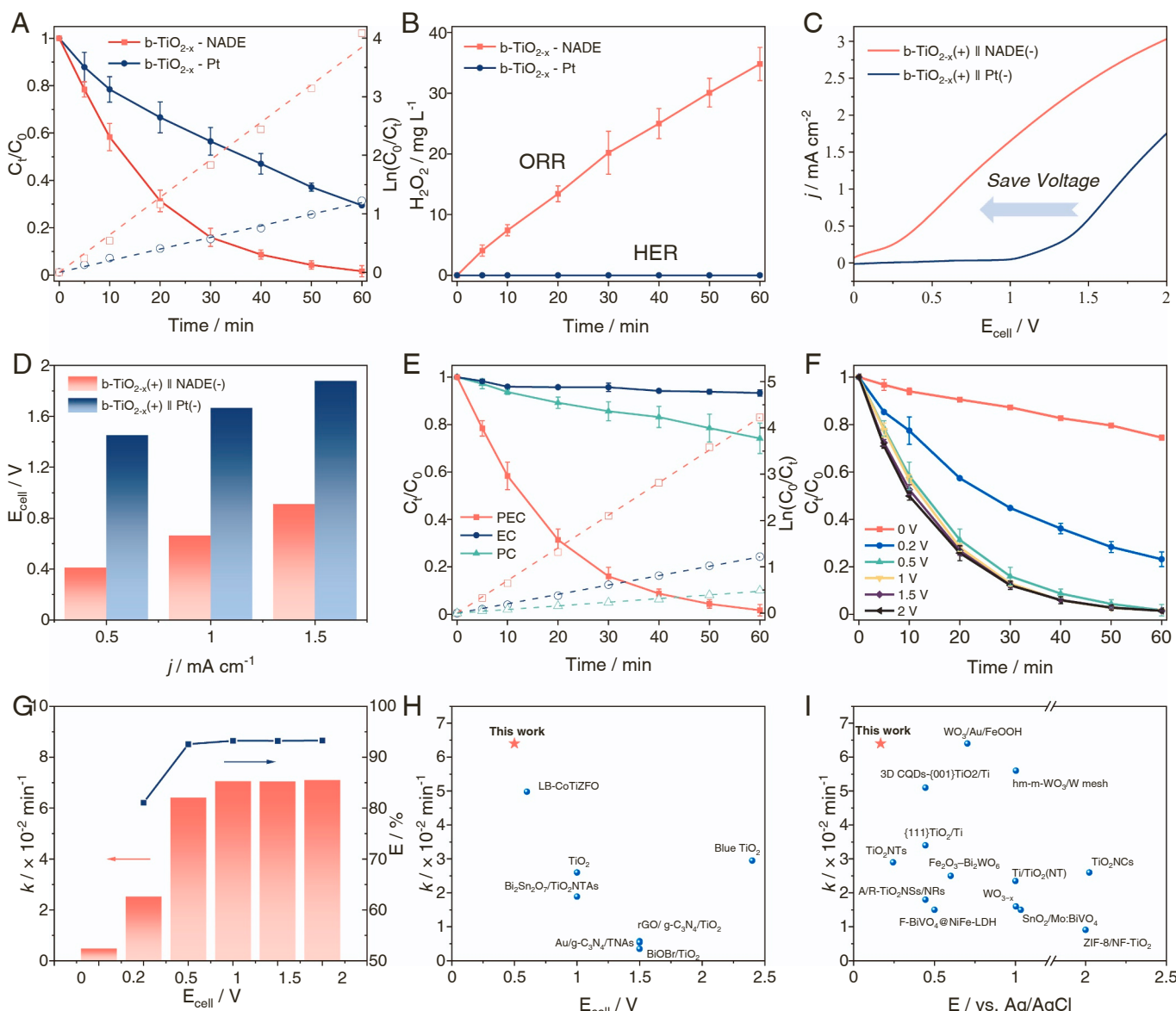


Fig. 3. (A) Degradation and reaction rate constant of SMT in b-TiO_{2-x} /NADE and b-TiO_{2-x} /Pt PEC systems. (B) H_2O_2 production in b-TiO_{2-x} /NADE and b-TiO_{2-x} /Pt PEC systems. Comparison of (C) LSV curves and (D) overpotentials at different current densities for b-TiO_{2-x} /NADE and b-TiO_{2-x} /Pt PEC systems. (E) Performance of the b-TiO_{2-x} /NADE system for contaminant SMT degradation under EC, PC, and PEC conditions. (F) Effect of different applied cell voltage on SMT removal in b-TiO_{2-x} /NADE PEC system. (G) The reaction rate constant and the extent of electrochemical enhancement at different applied cell voltage. Comparison of water purification performance under (H) applied cell voltage and (I) applied bias voltage with the last five years reported PEC water purification literatures.

nanocones photoanode and NADE cathode achieved efficient PEC water purification and higher H₂O₂ production.

Considering the fact that the reduction potential of two-electron ORR to H₂O₂ is more positive than that of HER to H₂, thermodynamic advantages can be identified in b-TiO_{2-x}/NADE PEC system. In order to prove the thermodynamic advantages of this system, PEC systems with two different cathode configurations were constructed. Intuitively, the catalytic activity can be reflected by comparing LSV curves. Fig. 3C showed that the LSV curve of b-TiO_{2-x}/NADE PEC system obviously shifted to the negative direction compared with that of b-TiO_{2-x}/Pt PEC system. Specifically, our PEC system only required the cell voltages of 0.41, 0.66, and 0.91 V to reach the current density of 0.5, 1, and 1.5 mA cm⁻², respectively, whereas relatively higher voltages of 1.45, 1.67, and 1.88 V were required in the traditional PEC system (Fig. 3D). These results proved that our b-TiO_{2-x}/NADE PEC system needed less electric energy, revealing noticeable thermodynamic advantages.

The EC, PC, and PEC process for SMT degradation were carried out at an applied cell voltage of 0.5 V (Fig. 3E). The EC process exhibited a negligible degradation efficiency of SMT (6.67%, 0.001 min⁻¹, 60 min), and the degradation efficiency of the PC process also remained poor (25.84%, 0.005 min⁻¹, 60 min). Nevertheless, the PEC degradation efficiency of b-TiO_{2-x}/NADE (98.32%, 0.064 min⁻¹, 60 min) was noticeably higher than the total degradation efficiency of EC and PC processes, suggesting a synergistic effect in the b-TiO_{2-x} photoanode between the electrocatalysis and photocatalysis. As evaluated by the synergy factor (SF) according to Eq. (6) [47],

$$SF = \left(\frac{k_{PEC}}{k_{EC} + k_{PC}} - 1 \right) \times 100\% \quad (6)$$

where k_{PEC} , k_{PC} , and k_{EC} are the reaction rate constant in PEC, PC, and EC process, respectively, the SF of b-TiO_{2-x} photoanode can reach to 967%. The high synergy factor indicates that the photogenerated electron-hole pairs separation (from photocatalysis) is greatly promoted by the applied potential (from electrocatalysis).

In PEC system, it was reported that an applied bias voltage could promote the separation and transfer of electron-hole pairs on photoanode, improving the PEC degradation performance. The effect of bias voltage on PEC degradation performance was further examined (Fig. 3F). With the applied cell voltage rise from 0 to 0.5 V, the removal efficiency was improved from 25.52% to 98.32% along with corresponding PEC k -value from 0.005 to 0.064 min⁻¹ (Fig. 3F and Fig. S7). When the applied cell voltage was further gradually improved to 2 V, no significant improvement was observed in degradation efficiency and PEC reaction rate constant compared with 0.5 V. Meanwhile, the extent of the electrochemical enhancement (E) can be calculated based on Eq. (7) [48]:

$$E = \frac{k_{PEC} - k_{PC}}{k_{PEC}} \times 100\% \quad (7)$$

where k_{PEC} and k_{PC} are the k -value in PEC and PC degradation of SMT, respectively. When the applied cell voltage rose from 0.2 to 0.5 V, the E-value was increased from 81.08% to 92.56% (Fig. 3G). While the E-values were 93.24%, 93.23% and 93.28% when the cell voltage were 1.0, 1.5 and 2.0 V respectively, resulted in no significant enhancement compared with 0.5 V (Fig. 3G). Herein, only 0.5 V cell voltage was required to drive its efficient PEC water purification thanks to the thermodynamic advantages of b-TiO_{2-x}/NADE PEC system.

To obtain a more intuitive understanding of the catalytic performance of our b-TiO_{2-x}/NADE PEC system, a comprehensive summary of the PEC water purification performance among the last five years reported photoanodes was exhibited in Figs. 3H and 3I. The comparison of reaction rate constant and applied voltage demonstrated that our b-TiO_{2-x}/NADE PEC system achieved better water purification performance under a lower voltage (0.5 V or 0.167 V vs. Ag/AgCl), surpassing other photoanodes. Thus, comparing to the existing research, this work

offers a novel integration between the b-TiO_{2-x} photoanode and the NADE cathode, making full use of the thermodynamic advantages, and achieving the cost-effective water purification.

3.3. Enhanced H₂O₂ production on b-TiO_{2-x} photoanode

To further prove the perfect integration of PEC water purification with EC H₂O₂ production by b-TiO_{2-x}/NADE system, the conventional anode (DSA and Pt) was respectively applied as the control experiments, while only 5.2% and 17.37% of SMT could be removed along with negligible H₂O₂ production at 0.5 V (Fig. 4A and Fig. S8). When the cell voltage was increased to 1.5 V, conventional anode exhibited improved degradation performance (38.7% of Pt and 70.49% of DSA) and H₂O₂ production (1.48 mg L⁻¹ of Pt and 32.13 mg L⁻¹ of DSA), while it was still far below 135.46 mg L⁻¹ H₂O₂ of b-TiO_{2-x} photoanode (Fig. 4A and Fig. S9). Intuitively, the synergistic effect of PC and EC process enabled PEC process a higher current density (Fig. 4B). Replacing dark anode with b-TiO_{2-x} photoanode also greatly reduced the high voltage requirement of water purification and H₂O₂ production due to the reduced Fermi level difference between the photoanode and the cathode (Fig. S10) [49]. The H₂O₂ production under different processes tended to be consistent with pollutant removal and current density. Impressively, the b-TiO_{2-x}/NADE PEC system showed an exceptional H₂O₂ production (6.83 μmol/h/cm²) and current efficiency (79.37%) with the lowest applied voltage (0.5 V) among the recently reported dual-functional PEC system (Table S4), surpassing obviously the previous reported a-Fe₂O₃/GDE dual-functional PEC system that only achieved H₂O₂ production (2.35 μmol/h/cm²) and current efficiency (32.5%) with 0.5 V vs Ag/AgCl applied bias [50]. More importantly, compared with traditional carbon black/PTFE cathode, NADE enables the molecular oxygen in the air to naturally diffuse into the reaction interface, where any aeration equipment and energy consumption for aeration is unnecessary, providing the prerequisite of low-consumption PEC water purification and H₂O₂ production.

The origin of this efficient H₂O₂ production of b-TiO_{2-x}/NADE PEC system should be further discussed from the following two aspects. On the one hand, anode photovoltage compensation conferred a more negative cathode potential for reducing O₂ to H₂O₂. Fig. 4C showed the change of the potential distribution of anode potential (E_{anode}) and cathode potential ($E_{cathode}$) as a function of cell voltage (E_{cell}). With an increase of E_{cell} , the PEC system and EC system had different performance in voltage distribution. To be more specific, in these two systems, $E_{cathode}$ (under PEC condition) and E_{anode} (under EC condition) increased rapidly and were distributed more voltage respectively. For example, when E_{cell} was constant (0.5 V), the $E_{cathode}$ for H₂O₂ production was then indirectly compensated by anode photovoltage, leading to its decrease from -0.06 V vs. Ag/AgCl (under EC condition) to -0.33 V vs. Ag/AgCl (under PEC condition) (Fig. 4C). Meanwhile, when E_{cell} increased from 0.2 V to 2.0 V, the anode photovoltage compensation rose from 0.13 V (under 0.2 V) to the peak of 0.63 V (under 1.5 V), and then slightly declined to 0.53 V (under 2 V) (Fig. 4C). This variation trend can be explained by the fact that PEC system is transformed from electro-assisted PC to photoassisted EC with the growth of E_{cell} , in which higher applied voltages result in a weaker anode photovoltage compensation [51].

On the other hand, the electron transfer in the PEC system was detected through open circuit potential test and $J-t$ curve [52]. After the addition of SMT in PEC system, the open circuit potential shifted positively by about 0.014 V (Fig. 4D), indicating that more electrons transfer to cathode for H₂O₂ production, and ultimately reduced the potential of photoanode [52]. Furthermore, the introduction of SMT made the current density further enlarged. Specifically, the introduction of SMT resulted in the enhancement of the photocurrent density from around 0.28–0.31 mA cm⁻² at 0.5 V (Fig. 4E). This inference was further validated by the H₂O₂ production comparison as depicted in Fig. 4F, where the H₂O₂ concentration in PEC system with SMT (34.8 mg L⁻¹) is higher

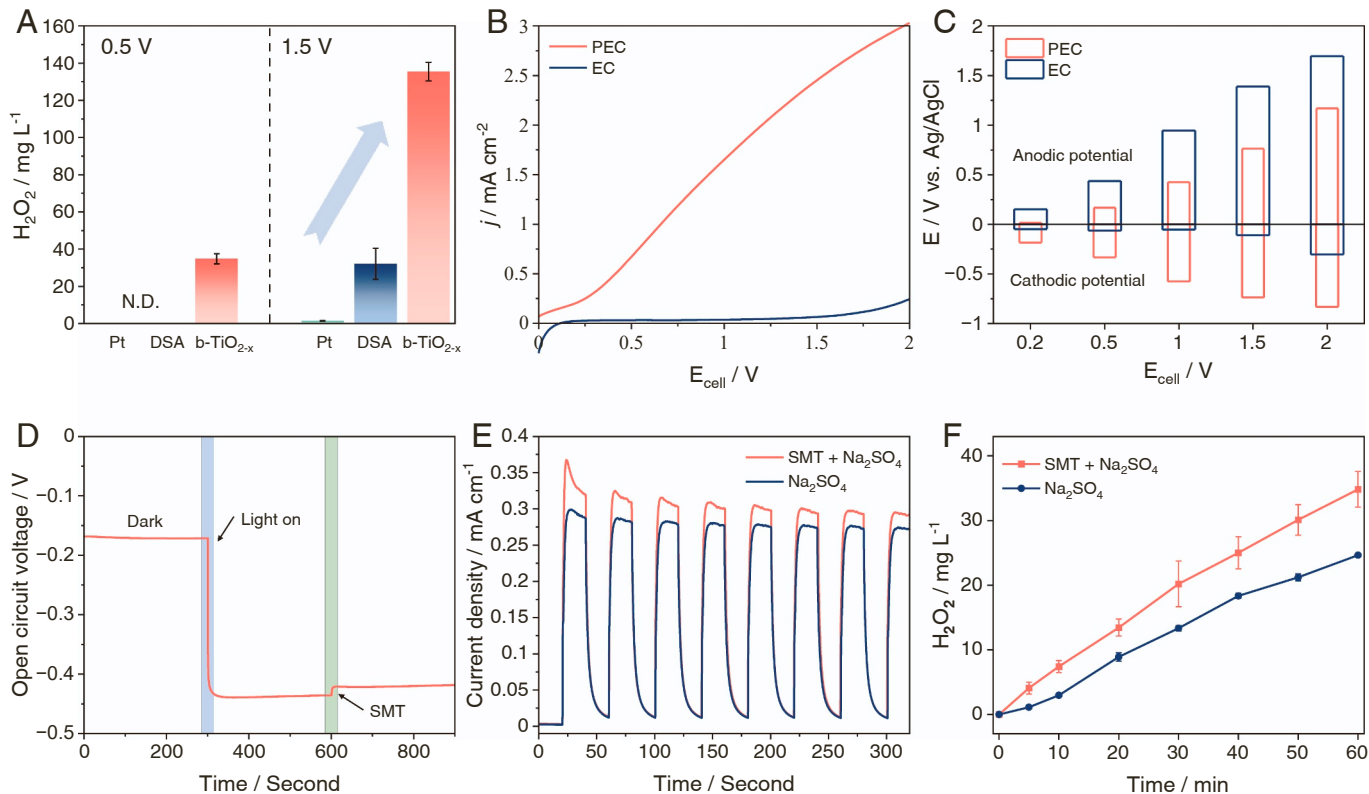


Fig. 4. (A) Comparison of cathodic H_2O_2 production with different materials as anode. (B) LSV curves of PEC and EC system. (C) Variation of potential distribution of E_{anode} and E_{cathode} as a function of E_{cell} in $\text{b-TiO}_{2-x}/\text{NADE}$ EC and PEC system. (D) Change of open circuit potential after adding pollutant. (E) Photocurrent density and (F) H_2O_2 production in pollutant-present and pollutant-absent conditions.

than that with only Na_2SO_4 (24.6 mg L^{-1}). This increase could be further attributed to the rapid capture of holes and its derivate $\cdot\text{OH}$ by pollutant [53], resulting in more electrons available for H_2O_2 generation.

Thus, anode photovoltage compensation and the introduction of pollutant (SMT), as two-layered factors, influence the production of H_2O_2 , not only O_2 molecule easily overcoming the reaction energy barrier for 2e^- ORR to H_2O_2 , but also more electrons being provided in PEC system.

3.4. Catalytic mechanism of the b-TiO_{2-x} photoanode

3.4.1. Involvement of oxygen vacancy for enhanced $\cdot\text{OH}$ generation

In order to further verify the importance of oxygen vacancy on the PEC reaction process, we respectively chose b-TiO_{2-x} and TiO_2 as photoanode to conduct PEC degradation. As depicted in Fig. 5A, both two photoanodes were active in degrading SMT under PEC condition. However, it removed 84.04% of SMT in b-TiO_{2-x} system over 30 min, which was significantly faster than TiO_2 (58.97%). Notably, when the degradation reaction continued to 60 min, SMT with a degradation efficiency of 98.32% and k -value of 0.064 min^{-1} was obtained in the b-TiO_{2-x} system, which were still higher than those of TiO_2 with a degradation efficiency of 88.36% and k -value of 0.034 min^{-1} (Fig. 5A and Fig. S12). This indicated that b-TiO_{2-x} performed better than TiO_2 in degrading pollutants in PEC system due to the introduction of oxygen vacancy.

It has been reported that there are usually two possible paths for the removal of contaminants (direct holes oxidation and indirect $\cdot\text{OH}$ oxidation) in PEC system for water purification [17]. To further confirm the main pathway of SMT degradation, we carried out quenching experiments using isopropanol (IPA) and ethylenediaminetetraacetic acid disodium (Na_2EDTA) as the quenchers of $\cdot\text{OH}$ and hole respectively. As

indicated by Fig. S13, the degradation efficiency of SMT decreased with the increase of IPA and Na_2EDTA concentration. When excessive Na_2EDTA was added into the reaction system, the degradation efficiency significantly dropped to 23.93% with k -value of 0.005 min^{-1} (Fig. 5B), suggesting the key role of hole. Furthermore, on adding excessive IPA into the reaction system for quenching $\cdot\text{OH}$, the degradation efficiency also significantly decreased to 27.92% with k -value of 0.006 min^{-1} (Fig. 5B), which basically had the same effect as quenching holes. Since the well-known fact that $\cdot\text{OH}$ usually results from water oxidation by holes, these results reveal that the PEC degradation process on b-TiO_{2-x} is dominated by indirect $\cdot\text{OH}$ oxidation, where holes are mainly responsible for H_2O oxidation to $\cdot\text{OH}$.

In order to validate the results of quenching experiment and the key role of oxygen vacancies, we further explored the reactive oxygen species (ROS) of the SMT degradation over b-TiO_{2-x} and TiO_2 by EPR measurement and quantitative experiment. Fig. 5C showed the EPR spectra of b-TiO_{2-x} using DMPO as a trapping agent. No signal was detected under dark condition (0 min), whereas with the start and progress of PEC reaction, the characteristic peak of DMPO- $\cdot\text{OH}$ adduction with intensity of 1:2:2:1 appeared and became stronger, confirming that the $\cdot\text{OH}$ generation came from the water oxidation by holes (Fig. 5C). Similar peaks with much weaker radical signals were observed over TiO_2 , indicating a much weaker water oxidation reactivity over TiO_2 (Fig. 5D). This result was also testified by $\cdot\text{OH}$ quantitative experiments (Fig. 5E). The concentration of $\cdot\text{OH}$ produced by TiO_{2-x} ($30.7 \mu\text{M}$) was 3.35 times of that produced by TiO_2 ($9.16 \mu\text{M}$). At the same time, the trapping of holes can be illustrated by the characteristic EPR signals of TEMPO. The characteristic peak intensity of TEMPO over b-TiO_{2-x} significantly decreased with illuminate time, suggesting the concentration of TEMPO was lowered (Fig. 5F). Hence, these experimental results verified the generation of $\cdot\text{OH}$ and holes during the PEC degradation of SMT over b-TiO_{2-x} and TiO_2 photoanode, proving the

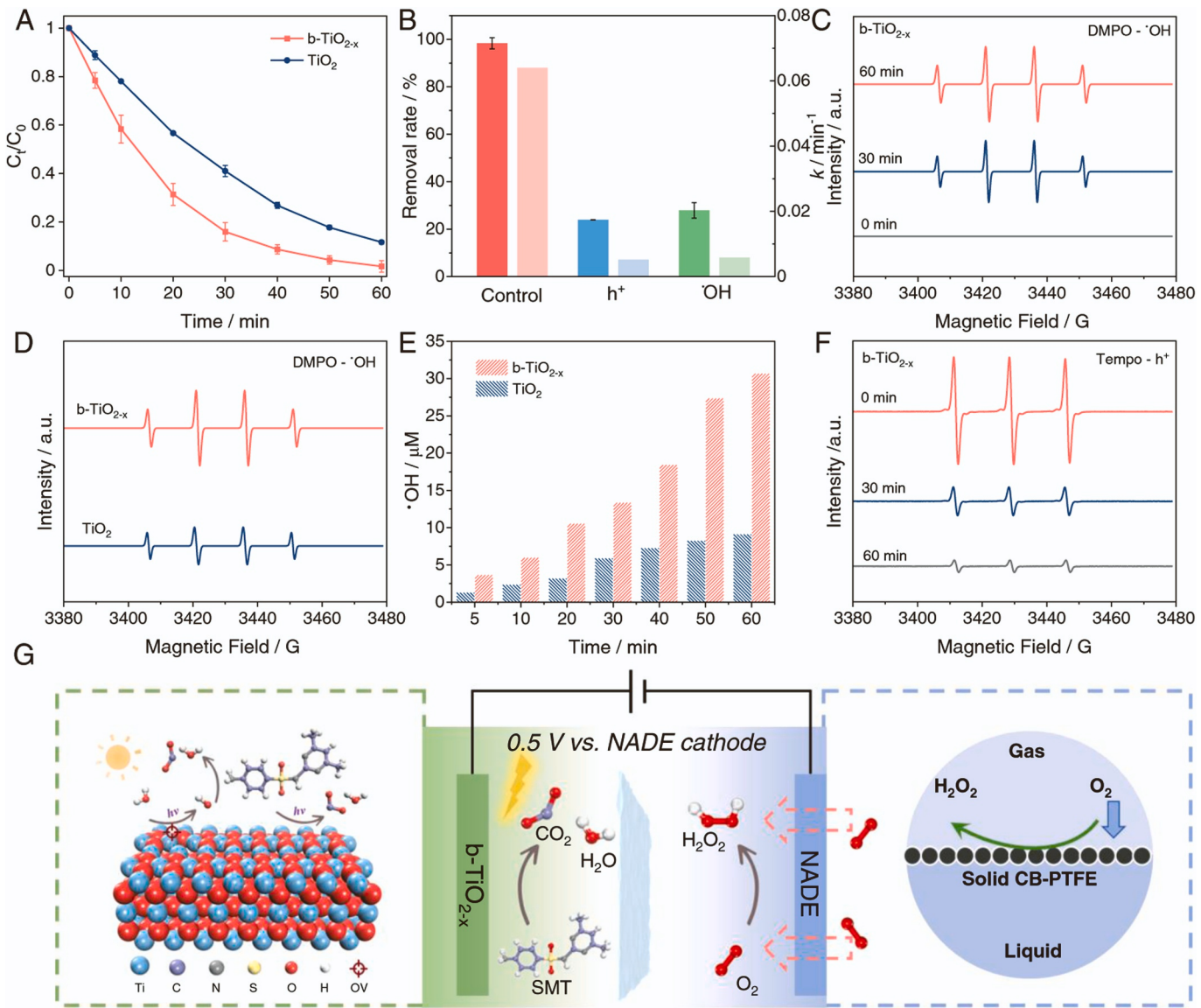


Fig. 5. (A) Comparison of water purification performance of PEC system with $b\text{-TiO}_{2-x}$ and TiO_2 as photoanode. (B) Degradation performance in quenching experiments. (C) EPR spectra of DMPO- $\cdot\text{OH}$ on $b\text{-TiO}_{2-x}$. (D) Comparison of EPR spectra of DMPO- $\cdot\text{OH}$ and (E) $\cdot\text{OH}$ quantitative concentration over $b\text{-TiO}_{2-x}$ and TiO_2 . (F) EPR spectra of TEMPO- h^+ over $b\text{-TiO}_{2-x}$. (G) Schematic illustration of PEC water purification on $b\text{-TiO}_{2-x}$ photoanode and H_2O_2 production on NADE.

involved effect of oxygen vacancy of TiO_{2-x} for enhanced $\cdot\text{OH}$ generation.

3.4.2. Enhanced charge separation and transfer of $b\text{-TiO}_{2-x}$

To further prove the mechanism of enhanced PEC performance after introducing oxygen vacancies, charge separation and transfer of $b\text{-TiO}_{2-x}$ were investigated, where PL measurements, photocurrent measurements, and EIS measurements were conducted as follows. First, the charge separation efficiency was investigated by PL measurements. As shown in Fig. 6A, the PL emission intensity of $b\text{-TiO}_{2-x}$ was significantly lower than that of TiO_2 , revealing the introduction of oxygen vacancies resulted in the inhibited recombination of electron and hole on $b\text{-TiO}_{2-x}$. Second, in J - t and LSV measurements, the $b\text{-TiO}_{2-x}$ exhibited the higher photocurrent than TiO_2 , further proving that the promoting effect of oxygen vacancies on the separation and transfer of photogenerated carriers (Fig. 6B and C). Third, EIS was conducted to disclose the interface charge transfer dynamics of photoanode. The charge transfer resistance value of TiO_2 ($13,087 \Omega$) was 25.5 times higher than that of $b\text{-TiO}_{2-x}$ (512.3Ω), indicating that the oxygen vacancies were greatly

conducive to reduce the interface charge transfer resistance (Fig. 6D).

Additionally, the ECSA was determined by measuring the C_{dl} . The C_{dl} value of $b\text{-TiO}_{2-x}$ ($2854.05 \mu\text{F cm}^{-2}$) was found to be much higher than that of TiO_2 ($36.83 \mu\text{F cm}^{-2}$), indicating oxygen vacancies allowed $b\text{-TiO}_{2-x}$ to have a larger ESCA and more active sites (Fig. 6E, F and Fig. S15) [54]. Besides, the surface charge injection efficiency ($\eta_{injection}$) of the photoanode was explored by a hole-scavenger-assisted PEC measurement, as $\eta_{injection}$ is correlated with the surface electron and hole recombination and surface reaction kinetics [55]. Compared to TiO_2 , the $\eta_{injection}$ of $b\text{-TiO}_{2-x}$ was improved, indicating more holes were utilized to achieve faster water oxidation to $\cdot\text{OH}$ kinetics (Fig. 6G). Moreover, the charge carrier density (N_d) of photoanode could be calculated based on the Mott-Schottky plots using Eq. (8) [54,56].

$$N_d = (2/e_0 \epsilon \epsilon_0 A^2) [d(1/C^2)/dE]^{-1} \quad (8)$$

where e_0 is the electron charge ($1.6 \times 10^{-19} \text{ C}$), ϵ is the dielectric constant of TiO_2 , ϵ_0 is the permittivity of vacuum ($8.86 \times 10^{-10} \text{ F/cm}$), A is the electrode area, C is the space charge layer capacity and E is the electrode potential. In this way, the $b\text{-TiO}_{2-x}$ exhibited a carrier density

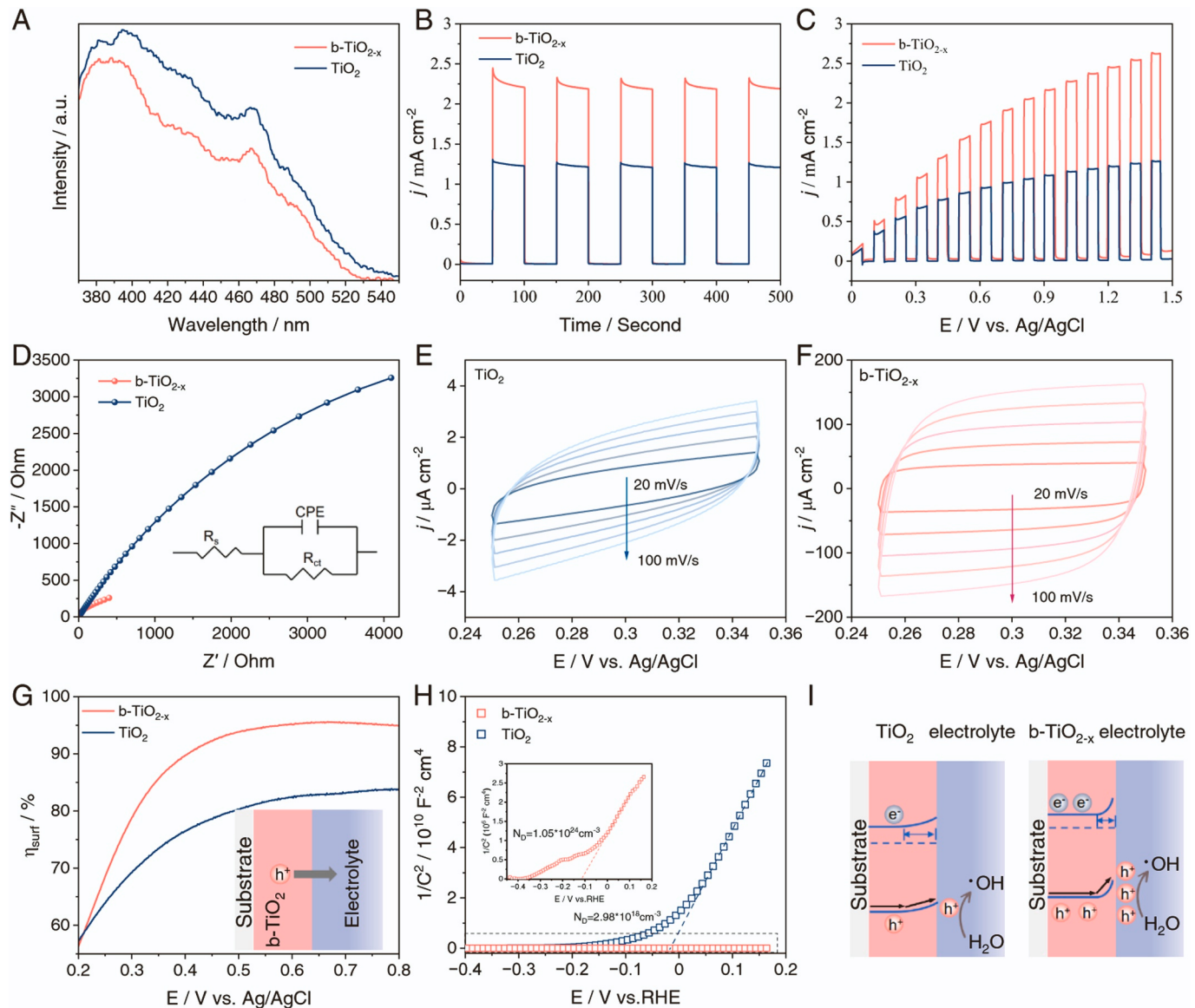


Fig. 6. (A) Steady-state PL spectra, (B) J-t curve, (C) LSV curve and (D) EIS Nyquist plots of TiO₂ and TiO_{2-x}. CV curves of (E) TiO₂ and (F) b-TiO_{2-x}. (G) η_{injection} of b-TiO_{2-x} and TiO₂. (H) Mott-Schottky curves. (I) Schematic illustration of interfacial electron transfer between photoanode and electrolyte.

of $1.05 \times 10^{24} \text{ cm}^{-3}$, which was approximately 5 orders of magnitude higher than that of TiO₂ ($2.98 \times 10^{18} \text{ cm}^{-3}$). It indicated that the introduction of oxygen vacancies induced the higher carrier concentration, where more holes were utilized to oxidize H₂O to •OH.

To summarize the above calculation and illustrate the significance of oxygen vacancies more intuitively, the schematic diagrams of the charge transfer process of TiO₂ and b-TiO_{2-x} photoanodes were displayed in Fig. 6I. When the photoanode is in contact with electrolyte, charge transfer takes place at the photoanode/electrolyte junction owing to the difference in redox potential of electrolyte and Fermi level of photoanode [57]. Subsequently, the charge distribution at the interface is changed by the charge transfer, resulting in bent band edges [57]. It is evident that bending degree relies on the initial difference between the Fermi level of photoanode and the electrolyte potential [57]. Due to this higher substantial difference of b-TiO_{2-x} compared with that of TiO₂, oxygen vacancies in b-TiO_{2-x} enable more band bending in the space charge region, where the enhanced electric field at the solid-liquid interface of b-TiO_{2-x} facilitates the electron-hole separation. Additionally, with the introduction of oxygen vacancies, the electron mobility, and charge carrier density can be improved accordingly, enabling that

more holes can be induced and transferred to the surface of b-TiO_{2-x} photoanode for oxidizing H₂O to •OH.

3.4.3. Theoretical calculation

Motivated by the aforementioned experiment results, we seek to further elucidate the enhanced •OH generation origin of b-TiO_{2-x} during PEC water purification process. There is a popular recognition that the generation of ROS is related to the surface electronic structure, adsorption sites, and reaction energy barrier of catalysis. Hence, DFT calculations were conducted to further examine the adsorption of the H₂O molecule on the photoanode surface and the further oxidation to •OH. On the basis of the above characterization results of photoanode, the theoretical models of b-TiO_{2-x} and TiO₂ were constructed correspondingly (Fig. S16).

Notably, the partial density of states (DOS) of Ti increased in the presence of oxygen vacancies, indicating oxygen vacancies could enable more titanium ion to be exposed and to increase the electronic contribution of Ti orbital to the total DOS (Fig. S17A and B) [58]. The total DOS results showed that the DOS near the Fermi level of b-TiO_{2-x} was remarkably higher than that of TiO₂ (Fig. S17C), proving that oxygen

vacancies further improved the charge transfer ability of the b-TiO_{2-x} [59], being consistent with the above EIS results. Further Bader charge analyses demonstrated that introducing oxygen vacancies could regulate the charge distribution of the Ti around it. The reduction of electron density of Ti in b-TiO_{2-x} (Fig. 7A) could assist in capturing negatively charged O atoms for adsorbing and activating H₂O molecules, and thus accelerating the •OH generation [60,61].

DFT calculations were further adopted to examine the adsorption of the H₂O molecule on the photoanode surface. Compared with TiO₂ (-0.354 eV), b-TiO_{2-x} (-0.722 eV) had a larger H₂O adsorption energy (Fig. 7B), indicating the stronger adsorption capacity of oxygen vacancies for H₂O. Moreover, we further assessed the hydrophilicity of photoanode by contact angle measurements. b-TiO_{2-x} was rather hydrophilic with a water contact angle of 14.3°, while that of TiO₂ was 20.4° (Fig. S18), confirming the stronger adsorption between H₂O molecule and oxygen vacancies. This rapid adsorption of H₂O molecules on the material surface provides a prerequisite for charge exchange with b-TiO_{2-x} photoanode. The charge density difference showed that more electrons transfer was clearly observed on b-TiO_{2-x} than that of TiO₂ after H₂O adsorption (Fig. 7C and Table S5) [62]. We further calculated the Gibbs free energy during the activation of H₂O. As the rate-determining step of activating H₂O to •OH, $\text{•OH}^+ + \text{h}^+ = \text{•OH}$, occurred with a significantly smaller reaction barrier of 1.28 eV over b-TiO_{2-x}, while that of TiO₂ was 2.42 eV (Fig. 7D) [30]. This indicated that b-TiO_{2-x} performed greatly in activating H₂O to •OH in thermodynamics due to oxygen vacancies, which was also coherent with the results of EPR measurement, quantitative experiments, degradation experiment and photoelectrochemical measurements.

3.5. Degradation pathway and toxicity assessment

To investigate the PEC degradation pathway of the contaminant SMT over b-TiO_{2-x} photoanode, the degradation intermediates of SMT were identified using liquid chromatography–mass spectrometry (LC-MS), and the mass spectra of the main intermediate products were shown in Fig. S19. Accordingly, four possible degradation pathways of SMT were

proposed (Fig. 8). To start with, SMT is easily hydroxylated to generate P1 due to the presence of •OH. Subsequently, P1 may undergo ring-opening reaction to form products P2, and the S–N bonds in P2 are broken by •OH to form P3 [63]. In another pathway, the N–C bond in pyrimidine ring of SMT are broken by single or synergistic attacks of holes and •OH to generate P4, and then P4 will be further transformed into P5 after hydroxylation [64]. The sulfonamide bond in sulfonamide antibiotics is easily broken by •OH and holes attacks. As a result, P6 and P7 are produced from the S–N bond cleavage of SMT. Then, the aniline group and easily oxidized methyl group in P6 were substituted and oxidized by •OH, respectively, resulting in the product P8 and P9. P7 can be oxidized into P5 and P3 by •OH. Besides, SMT may undergo smiles-type rearrangement followed by SO₂ extrusion, generating product P10, and further oxidized into product P11 [65]. Ultimately, the degradation intermediates were degraded to small molecules and mineralized into H₂O and CO₂, which is consistent with the obtained results from mineralization (Fig. S20).

Moreover, it is necessary to evaluate the toxicity of degradation intermediates during PEC degradation process. The software tool (T.E.S.T) based on the quantitative structure activity relationship (QSAR) was used to predict the growth inhibition (IGC50), acute toxicity (LC50–96 h) and mutagenicity of SMT and its intermediates. According to growth inhibition (IGC50) and acute toxicity LC50 of these intermediates, most of intermediates were less harmful than SMT except product P1 and P10, fortunately they could be further oxidized to lower toxicities intermediates (Fig. S21). Thus, the toxicity of SMT was greatly reduced during PEC degradation process.

3.6. Environmental application prospect of b-TiO_{2-x} / NADE PEC system

Generally, the environmental adaptability of the photoanode is crucial for environmental remediation. In order to test out PEC system, the following four aspects were examined. First, this PEC system excelled in degrading not only SMT but also other multiple refractory contaminants in wastewater, including tetracycline (TC, 95.11%, 0.049 min⁻¹), bisphenol A (BPA, 100%, 0.047 min⁻¹), phenol (BP, 91.54%,

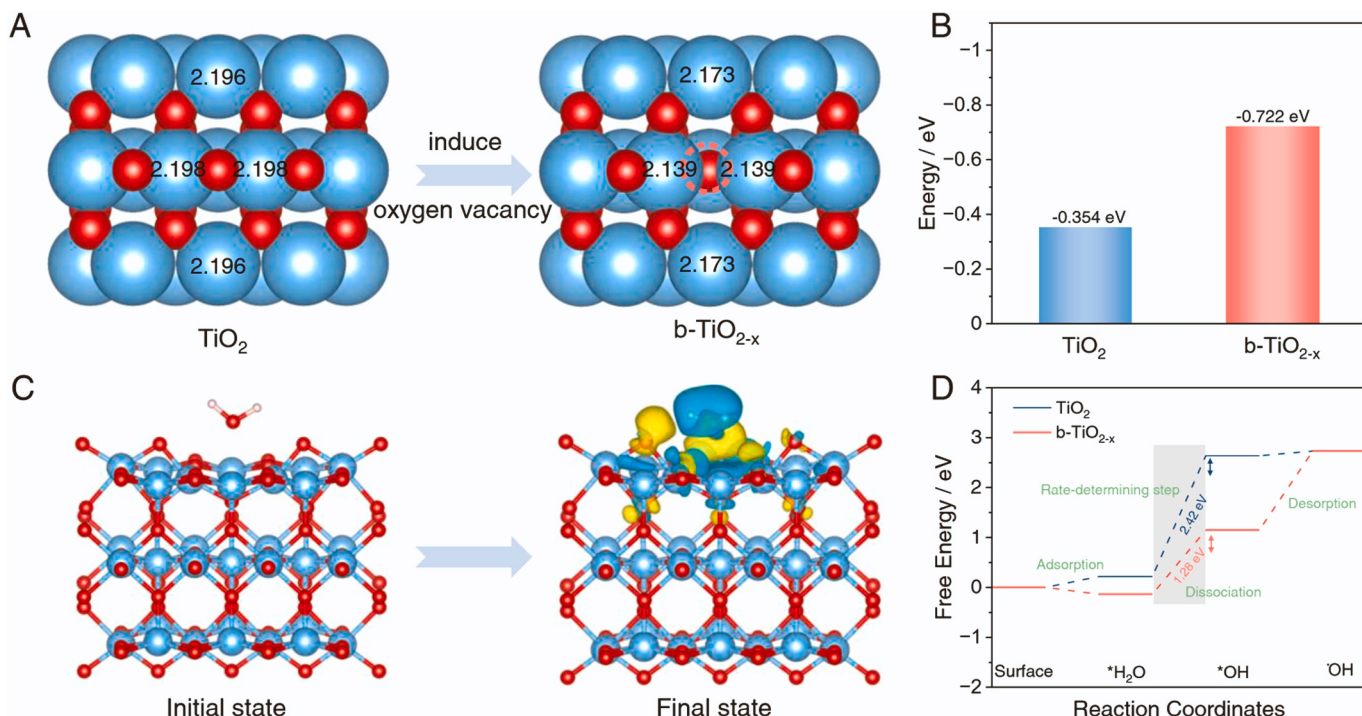


Fig. 7. (A) Bader charge analysis on TiO₂ and b-TiO_{2-x} model. (B) The adsorption energy of H₂O molecule on TiO₂ and b-TiO_{2-x}. (C) Charge density difference of H₂O molecule adsorption on b-TiO_{2-x}. (D) Free energy diagram for the formation of •OH on TiO₂ and b-TiO_{2-x}.

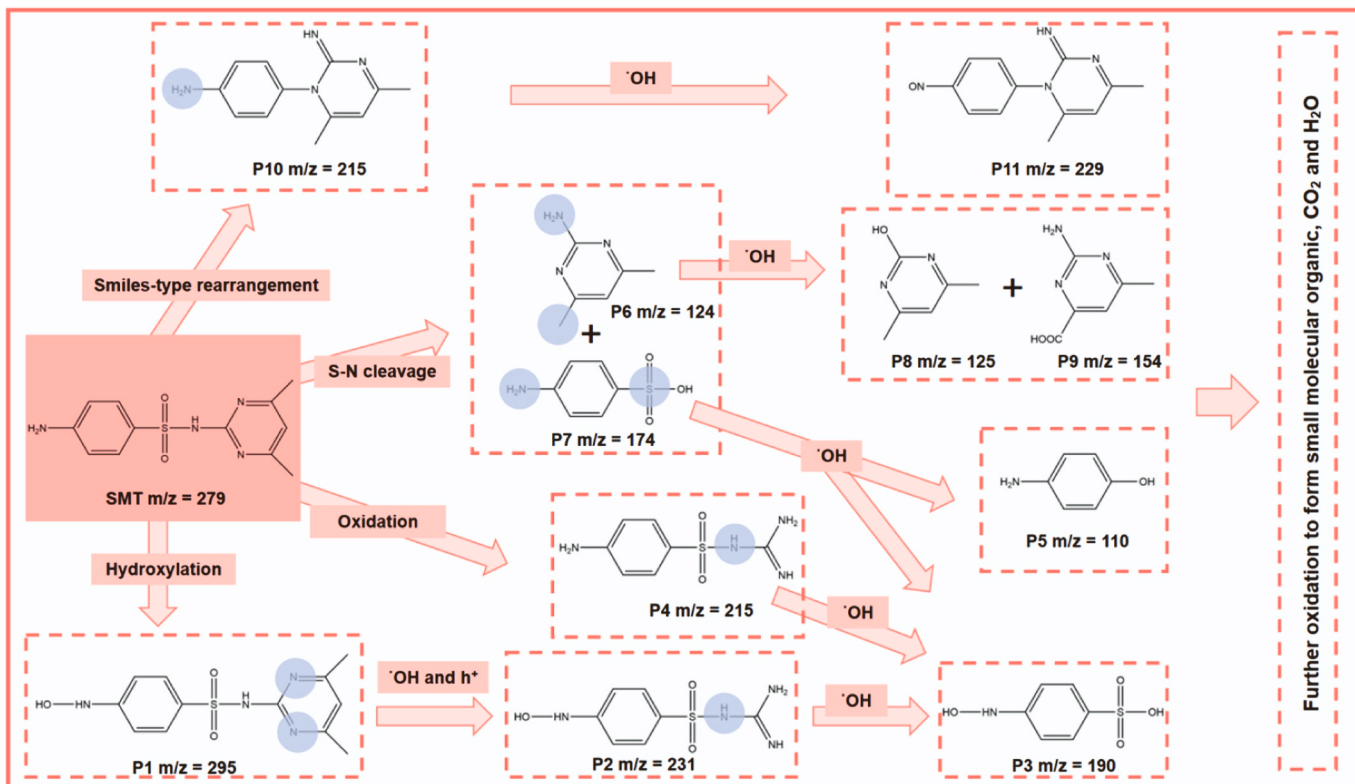


Fig. 8. Proposed degradation pathways of contaminant SMT in b-TiO_{2-x}/NADE PEC system.

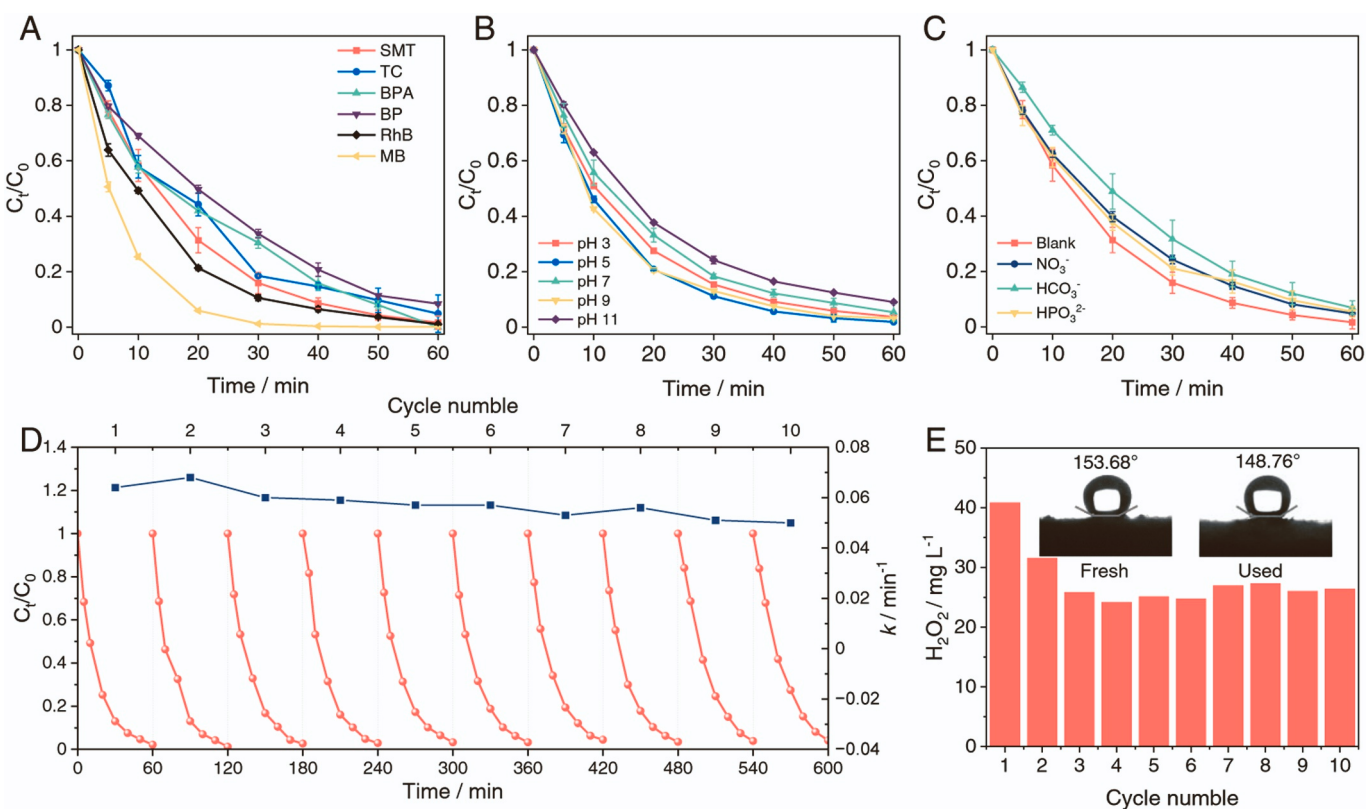


Fig. 9. (A) Removal of multiple pollutants in b-TiO_{2-x}/NADE PEC system. Effect of (B) pH and (C) background anions on SMT removal in b-TiO_{2-x}/NADE PEC system. Cyclic experiment of (D) SMT removal and (E) H_2O_2 production in b-TiO_{2-x}/NADE PEC system.

0.041 min^{-1}), rhodamine B (RhB, 98.92%, 0.072 min^{-1}) and methylene blue (MB, 99.88%, 0.138 min^{-1}) (Fig. 9A and Fig. S22), indicating its broad applicability. Besides, this PEC system displayed excellent pH stability and high degradation efficiency. As illustrated in the Fig. 9B and Fig. S23, within the pH range of 3–11, over 90% of SMT pollutants could be degraded, highlighting its extensive pH applicability. Moreover, it was found that inorganic anions in actual wastewater would react with free radicals, thus affecting the removal performance of the target pollutants. As shown in Fig. 9C and Fig. S24, all anions (NO_3^- , HCO_3^- , HPO_4^{2-}) more or less restrained the PEC degradation of SMT, where HCO_3^- exhibited a more negative effect on the degradation of SMT, with the corresponding degradation efficiency decreasing by 5.24%, and k -value decreasing from 0.064 min^{-1} to 0.042 min^{-1} . This result could be attributed to that HCO_3^- was reported to trap hole and $\cdot\text{OH}$, forming weaker free radicals $\cdot\text{CO}_3^-$ which hampered the degradation of SMT [66]. Noteworthily, even in such conditions when various anions are added, our PEC system still could degrade more than 93.1% of SMT. Apart from keeping high degradation efficiency in various environments, superior reusability of process is essential for practical water purification. After ten cycles of testing, the PEC system still displayed a degradation efficiency of 95%, and the H_2O_2 production could also reach to 26.39 mg L^{-1} (Fig. 9D and E). The morphology and crystal structure of b-TiO_{2-x} did not display significantly changes (Fig. S25), proving the recyclability and stability. The superhydrophobic three-phase interface of NADE was hardly any damage, with its contact angle changing slightly from 153.68° to 148.76° (Fig. 9E). Meanwhile, we further conducted the accelerated life test of b-TiO_{2-x} photoanode in acidic (0.5 M H₂SO₄) pH condition. The results showed that the photoanode still display excellent stability in the electrolyte of pH = 0 (Fig. S26). By comparing the SEM images of the photoanode before and after the accelerated life test, it was observed that the morphology of

b-TiO_{2-x} photoanode remained nanocone arrays structure and firmly grown on the Ti mesh substrate (Fig. S27A). The XRD patterns and XPS spectra had no obvious changes after the cyclic experiments (Fig. S27B-E), which also proved the stability of b-TiO_{2-x} photoanode. Herein, this novel PEC system exhibits great potential for practical environmental remediation and H_2O_2 production applications.

To achieve self-powered water purification and H_2O_2 production, the applicability of b-TiO_{2-x}/NADE PEC system was also explored under real outdoor sunlight illumination. We set up a solar-powered PEC system with a solar panel of 0–2 V. In this system, sunlight is utilized to not only activate b-TiO_{2-x} photoanode for water purification, but also illuminate the solar panel to provide a bias, which enables efficient PEC water purification and H_2O_2 production solely through the utilization of solar power and atmospheric O₂ for the first time, achieving zero electric energy consumption. Specifically, under real sunlight irradiation, this novel solar-powered PEC system exhibited excellent catalytic performance in degrading SMT (96.31%), CBZ (89.21%) and MB (99.13%) in anodic compartment, and achieving a H_2O_2 productivity of 29.9, 32.9 and 48.1 mg/L in cathodic compartment within 120 min respectively (Fig. 10A and B). Based on the discussion so far, the PEC system could achieve efficient water purification and H_2O_2 production under both laboratory and outdoor conditions. The economic feasibility was further analysis in Fig. 10C. The energy consumption of b-TiO_{2-x}/NADE PEC system was only 0.034 kWh/m^3 following from the Eq. S1 and Text S3, showing lower values than those in previous report [67]. More excitingly, when this system was subjected to actual solar, zero electric energy consumption was required. In addition, the simultaneous production of value-added H_2O_2 could fully compensate for the electric cost of the system, which even contributes to the overall profitability of 4.8 and 4.5 cents/m³ under laboratory and outdoor conditions respectively according to Eq. S2 and Text S3. Fig. 10D exhibits the complete

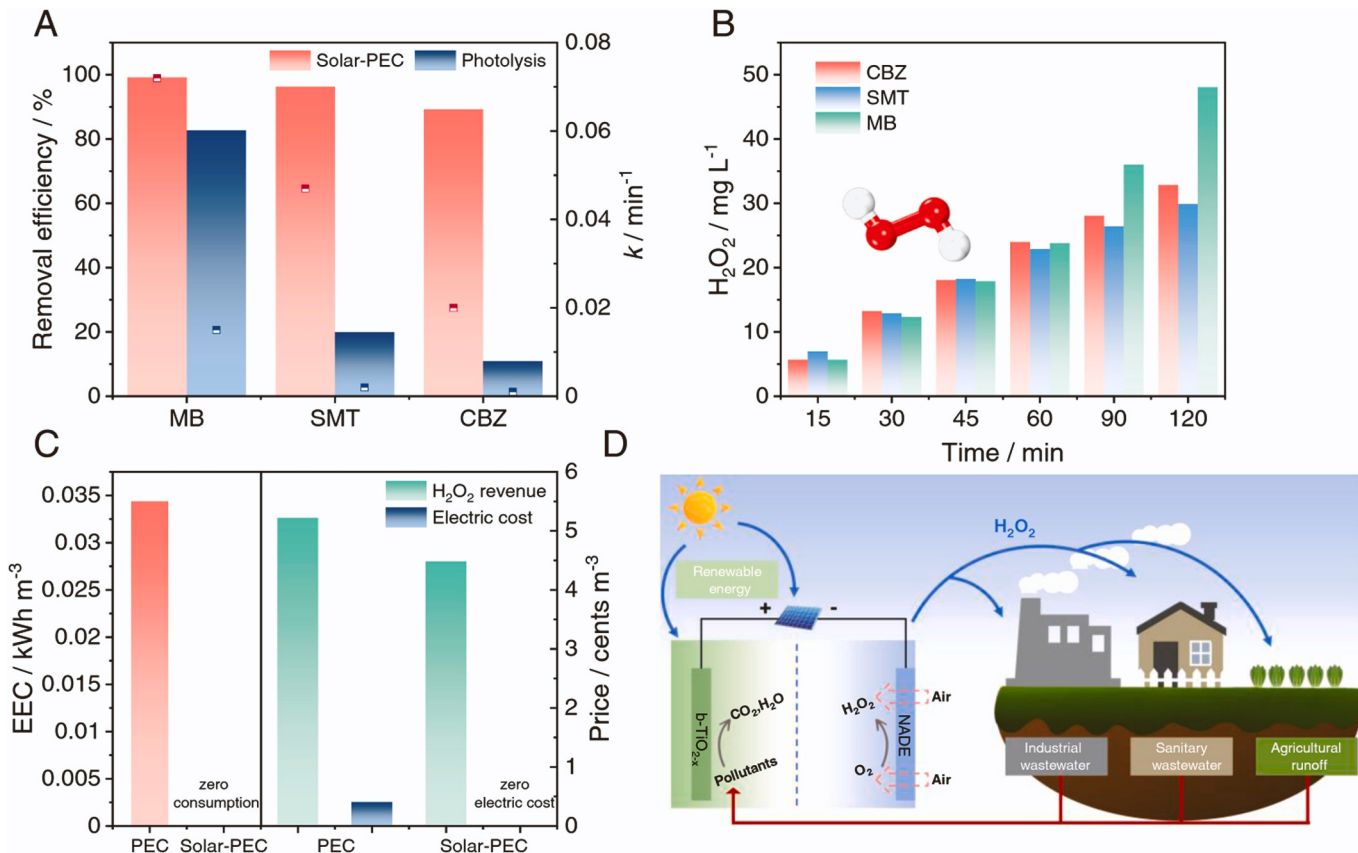


Fig. 10. b-TiO_{2-x}/NADE PEC system performance of (A) water purification and simultaneous (B) H_2O_2 production under real outdoor sunlight illumination. (C) The economic feasibility. (D) Dual-function PEC processing route from refractory wastewater to clean water and value-added H_2O_2 .

dual-function PEC processing route from refractory wastewater to clean water and value-added H₂O₂ with merely solar energy-driven reusable photoanode, requiring no additional oxidants, which ensures sustainable future energy demand and eco-environmental safety.

4. Conclusion

In summary, we report a high-efficiency and energy-saving PEC system coupling anodic water purification with cathodic H₂O₂ production. Compared to conventional PEC systems, our innovative design achieves remarkable results: a 98.32% removal of SMT at the b-TiO_{2-x} photoanode and a H₂O₂ production rate of 6.83 μmol/h/cm² at NADE, while operating at an ultra-low cell voltage of 0.5 V and consuming only 0.034 kWh/m³ of wastewater treated. The excellent performance of our PEC system in pollutant removal, H₂O₂ production, and the low applied voltage and energy consumption is beneficial from (1) our innovative cathode substitution strategies that Pt cathode is replaced by carbon cathode, with HER process replaced by 2e⁻ORR process; (2) the synergistic effect between photoanode and cathode, which not only allows O₂ molecule to overcome the reaction energy barrier for 2e⁻ORR to H₂O₂ more easily, but also provides more electrons for cathode; (3) the introduction of oxygen vacancies which not only modulate the charge carrier dynamics and band structure simultaneously, but also optimize the adsorption and activation energy barrier of H₂O, leading to enhanced •OH production. In addition, the practical utility of our PEC system is validated under real sunlight environment, in which no additional energy consumption is required for water purification and H₂O₂ production. Building upon these findings, this work not only elucidates the mechanisms underlying the enhanced pollutant degradation and H₂O₂ production in PEC system, but also demonstrates a cost-effective and environmental-benign route for water purification and resourcization.

CRediT authorship contribution statement

Shuaishuai Li: Validation, Data curation. **Xiuwu Zhang:** Validation, Data curation. **Minghua Zhou:** Writing – review & editing, Supervision, Funding acquisition, Conceptualization. **Ruiheng Liang:** Writing – original draft, Methodology, Investigation, Formal analysis. **Huizhong Wu:** Methodology, Investigation. **Zhongzheng Hu:** Methodology, Investigation. **Jiangli Sun:** Validation, Data curation. **Chunhong Fu:** Validation, Data curation.

Declaration of Competing Interest

The authors declare that they have no known competing financial interests or personal relationships that could have appeared to influence the work reported in this paper.

Data availability

Data will be made available on request.

Acknowledgements

This work was financially supported by National Key R&D Program International Cooperation Project (2023YFE0108100), Natural Science Foundation of China (nos. U23B20165 and 52170085), Key Project of Natural Science Foundation of Tianjin (no. 21JCZDJC00320), and Fundamental Research Funds for the Central Universities, Nankai University.

Appendix A. Supporting information

Supplementary data associated with this article can be found in the online version at doi:10.1016/j.apcatb.2024.124042.

References

- [1] P.H. Gleick, Water strategies for the next administration, *Science* 354 (2016) 555–556.
- [2] S. Rojas, P. Horcajada, Metal–Organic Frameworks for the removal of emerging organic contaminants in water, *Chem. Rev.* 120 (2020) 8378–8415.
- [3] J.R. Werber, C.O. Osuji, M. Elimelech, Materials for next-generation desalination and water purification membranes, *Nat. Rev. Mater.* 1 (2016) 16018.
- [4] K. Zuo, S. Garcia-Segura, G.A. Cerrón-Calle, F.-Y. Chen, X. Tian, X. Wang, X. Huang, H. Wang, P.J.J. Alvarez, J. Lou, M. Elimelech, Q. Li, Electrified water treatment: fundamentals and roles of electrode materials, *Nat. Rev. Mater.* 8 (2023) 472–490.
- [5] Y. He, K. Chen, M.K.H. Leung, Y. Zhang, L. Li, G. Li, J. Xuan, J. Li, Photo fuel Cell – A Rev., *Chem. Eng. J.* 428 (2022) 131074.
- [6] J.-A. Lin, I. Roh, P. Yang, Photochemical diodes for simultaneous bias-free glycerol valorization and hydrogen evolution, *J. Am. Chem. Soc.* 145 (2023) 12987–12991.
- [7] S. Xu, Q. Shen, J. Zheng, Z. Wang, X. Pan, N. Yang, G. Zhao, Advances in biomimetic photoelectrocatalytic reduction of carbon dioxide, *Adv. Sci.* 9 (2022) 2203941.
- [8] K. Poonia, P. Singh, A. Singh, S. Thakur, Q. Van Le, T. Ahamad, P. Raizada, C. Wang, L.H. Nguyen, V.-H. Nguyen, Photoelectrocatalytic systems for simultaneous energy recovery and wastewater treatment: a review, *Environ. Chem. Lett.* 21 (2023) 265–283.
- [9] X. Zong, H. Chen, B. Seger, T. Pedersen, M.S. Dargusch, E.W. McFarland, C. Li, L. Wang, Selective production of hydrogen peroxide and oxidation of hydrogen sulfide in an unbiased solar photoelectrochemical cell, *Energ. Environ. Sci.* 7 (2014) 3347–3351.
- [10] T. Wang, L. Tao, X. Zhu, C. Chen, W. Chen, S. Du, Y. Zhou, B. Zhou, D. Wang, C. Xie, P. Long, W. Li, Y. Wang, R. Chen, Y. Zou, X.-Z. Fu, Y. Li, X. Duan, S. Wang, Combined anodic and cathodic hydrogen production from aldehyde oxidation and hydrogen evolution reaction, *Nat. Catal.* 5 (2022) 66–73.
- [11] J. Qi, Y. Du, Q. Yang, N. Jiang, J. Li, Y. Ma, Y. Ma, X. Zhao, J. Qiu, Energy-saving and product-oriented hydrogen peroxide electrosynthesis enabled by electrochemistry pairing and product engineering, *Nat. Commun.* 14 (2023) 6263.
- [12] W.-J. Liu, Z. Xu, D. Zhao, X.-Q. Pan, H.-C. Li, X. Hu, Z.-Y. Fan, W.-K. Wang, G.-H. Zhao, S. Jin, G.W. Huber, H.-Q. Yu, Efficient electrochemical production of glucaric acid and H₂ via glucose electrolysis, *Nat. Commun.* 11 (2020) 265.
- [13] Z. Zheng, D. Wu, L. Chen, S. Chen, H. Wan, G. Chen, N. Zhang, X. Liu, R. Ma, Collaborative optimization of thermodynamic and kinetic for Ni-based hydroxides in electrocatalytic urea oxidation reaction, *Appl. Catal. B Environ.* 340 (2024) 123214.
- [14] Q. Zhang, F.M.D. Kazim, S. Ma, K. Qu, M. Li, Y. Wang, H. Hu, W. Cai, Z. Yang, Nitrogen dopants in nickel nanoparticles embedded carbon nanotubes promote overall urea oxidation, *Appl. Catal. B Environ.* 280 (2021) 119436.
- [15] S. Qu, H. Wu, Y.H. Ng, Clean production of hydrogen peroxide: a heterogeneous solar-driven redox process, *Adv. Energy Mater.* 13 (2023) 2301047.
- [16] Y. Zhang, K. Xie, F. Zhou, F. Wang, Q. Xu, J. Hu, H. Ding, P. Li, Y. Tan, D. Li, J. Zhu, H. Zhou, C. Zhao, S. Lin, Y. Wu, Electrochemical oxygen generator with 99.9% oxygen purity and high energy efficiency, *Adv. Energy Mater.* 12 (2022) 2201027.
- [17] R. Song, H. Chi, Q. Ma, D. Li, X. Wang, W. Gao, H. Wang, X. Wang, Z. Li, C. Li, Highly efficient degradation of persistent pollutants with 3D nanocane TiO₂-based photoelectrocatalysis, *J. Am. Chem. Soc.* 143 (2021) 13664–13674.
- [18] Y. Feng, H.H.M. Rijnaarts, D. Yntema, Z. Gong, D.D. Dionysiou, Z. Cao, S. Miao, Y. Chen, Y. Ye, Y. Wang, Applications of anodized TiO₂ nanotube arrays on the removal of aqueous contaminants of emerging concern: a review, *Water Res* 186 (2020) 116327.
- [19] M.S. Koo, K. Cho, J. Yoon, W. Choi, Photoelectrochemical degradation of organic compounds coupled with molecular hydrogen generation using electrochromic TiO₂ nanotube arrays, *Environ. Sci. Technol.* 51 (2017) 6590–6598.
- [20] C. Chen, Y. Wei, G. Yuan, Q. Liu, R. Lu, X. Huang, Y. Cao, P. Zhu, Synergistic effect of Si doping and heat treatments enhances the photoelectrochemical water oxidation performance of TiO₂ nanorod arrays, *Adv. Funct. Mater.* 27 (2017) 1701575.
- [21] R. Tang, S. Zhou, Z. Yuan, L. Yin, Metal–Organic Framework derived Co₃O₄/TiO₂/Si heterostructured nanorod array photoanodes for efficient photoelectrochemical water oxidation, *Adv. Funct. Mater.* 27 (2017) 1701102.
- [22] Q. Pan, A. Li, Y. Zhang, Y. Yang, C. Cheng, Rational design of 3D hierarchical ternary SnO₂/TiO₂/BiVO₄ arrays photoanode toward efficient photoelectrochemical performance, *Adv. Sci.* 7 (2020) 1902235.
- [23] P. Zhang, T. Wang, X. Chang, L. Zhang, J. Gong, Synergistic cocatalytic effect of carbon nanodots and Co₃O₄ nanoclusters for the photoelectrochemical water oxidation on hematite, *Angew. Chem. Intern. Ed.* 55 (2016) 5851–5855.
- [24] L. Luo, W. Chen, S.-M. Xu, J. Yang, M. Li, H. Zhou, M. Xu, M. Shao, X. Kong, Z. Li, H. Duan, Selective photoelectrocatalytic glycerol oxidation to dihydroxyacetone via enhanced middle hydroxyl adsorption over a Bi₂O₃-incorporated catalyst, *J. Am. Chem. Soc.* 144 (2022) 7720–7730.
- [25] Z. Li, L. Luo, M. Li, W. Chen, Y. Liu, J. Yang, S.-M. Xu, H. Zhou, L. Ma, M. Xu, X. Kong, H. Duan, Photoelectrocatalytic C–H halogenation over an oxygen vacancy-rich TiO₂ photoanode, *Nat. Commun.* 12 (2021) 6698.
- [26] K. Sharma, A. Kumar, T. Ahamad, Q.V. Le, P. Raizada, A. Singh, L.H. Nguyen, S. Thakur, V.-H. Nguyen, P. Singh, Sulphur vacancy defects engineered metal sulfides for amended photo(electro)catalytic water splitting: a review, *J. Mater. Sci. Technol.* 152 (2023) 50–64.
- [27] K.H. Kim, C.-W. Choi, S. Choung, Y. Cho, S. Kim, C. Oh, K.-S. Lee, C.-L. Lee, K. Zhang, J.W. Han, S.-Y. Choi, J.H. Park, Continuous oxygen vacancy gradient in

- TiO₂ photoelectrodes by a photoelectrochemical-driven "Self-Purification" process, *Adv. Energy Mater.* 12 (2022) 2103495.
- [28] S. Wang, P. Chen, J.-H. Yun, Y. Hu, L. Wang, An electrochemically treated BiVO₄ photoanode for efficient photoelectrochemical water splitting, *Angew. Chem. Intern. Ed.* 56 (2017) 8500–8504.
- [29] Z. Wang, X. Mao, P. Chen, M. Xiao, S.A. Monny, S. Wang, M. Konarova, A. Du, L. Wang, Understanding the roles of oxygen vacancies in Hematite-based photoelectrochemical processes, *Angew. Chem. Intern. Ed.* 58 (2019) 1030–1034.
- [30] J. Wu, Y. Tao, C. Zhang, Q. Zhu, D. Zhang, G. Li, Activation of chloride by oxygen vacancies-enriched TiO₂ photoanode for efficient photoelectrochemical treatment of persistent organic pollutants and simultaneous H₂ generation, *J. Hazard. Mater.* 443 (2023) 130363.
- [31] Y. Mao, P. Wang, L. Li, Z. Chen, H. Wang, Y. Li, S. Zhan, Unravelling the synergy between oxygen vacancies and oxygen substitution in BiO_{2-x} for efficient molecular-oxygen activation, *Angew. Chem. Intern. Ed.* 59 (2020) 3685–3690.
- [32] S. Zhan, H. Zhang, X. Mi, Y. Zhao, C. Hu, L. Lyu, Efficient Fenton-like process for pollutant removal in electron-rich/poor reaction sites induced by surface oxygen vacancy over cobalt-zinc oxides, *Environ. Sci. Technol.* 54 (2020) 8333–8343.
- [33] T. Zhou, L. Li, J. Li, J. Wang, J. Bai, L. Xia, Q. Xu, B. Zhou, Electrochemically reduced TiO₂ photoanode coupled with oxygen vacancy-rich carbon quantum dots for synergistically improving photoelectrochemical performance, *Chem. Eng. J.* 425 (2021) 131770.
- [34] Z. Tian, Y. Da, M. Wang, X. Dou, X. Cui, J. Chen, R. Jiang, S. Xi, B. Cui, Y. Luo, H. Yang, Y. Long, Y. Xiao, W. Chen, Selective photoelectrochemical oxidation of glucose to glucaric acid by single atom Pt decorated defective TiO₂, *Nat. Commun.* 14 (2023) 142.
- [35] Q. Zhang, M. Zhou, G. Ren, Y. Li, Y. Li, X. Du, Highly efficient electrosynthesis of hydrogen peroxide on a superhydrophobic three-phase interface by natural air diffusion, *Nat. Commun.* 11 (2020) 1731.
- [36] R.M. Sellers, Spectrophotometric determination of hydrogen peroxide using potassium titanium(IV) oxalate, *Analyst* 105 (1980) 950–954.
- [37] Q. Zhang, H. Yin, P. Su, W. Fu, G. Song, M. Zhou, Insight into the dual-cathode peroxy-coagulation process for cost-effective treatment of organic wastewater: increase pH application range and reduce iron sludge, *Chem. Eng. J.* 444 (2022) 136590.
- [38] G. Kresse, J. Furthmüller, Efficiency of ab-initio total energy calculations for metals and semiconductors using a plane-wave basis set, *Comp. Mater. Sci.* 6 (1996) 15–50.
- [39] G. Kresse, J. Furthmüller, Efficient iterative schemes for ab initio total-energy calculations using a plane-wave basis set, *Phys. Rev. B* 54 (1996) 11169–11186.
- [40] J.P. Perdew, K. Burke, M. Ernzerhof, Generalized gradient approximation made simple, *Phys. Rev. Lett.* 77 (1996) 3865–3868.
- [41] Q. Ma, R. Song, F. Ren, H. Wang, W. Gao, Z. Li, C. Li, Photoelectrocatalytic degradation of refractory pollutants over WO₃/W network photoelectrode with heterophase junction for enhancing mass transportation and charge separation, *Appl. Catal. B Environ.* 309 (2022) 121292.
- [42] F. Yang, X. Bao, P. Li, X. Wang, G. Cheng, S. Chen, W. Luo, Boosting hydrogen oxidation activity of Ni in alkaline media through oxygen-vacancy-rich CeO₂/Ni heterostructures, *Angew. Chem. Int. Ed.* 58 (2019) 14179–14183.
- [43] Q. Ren, Y. He, H. Wang, Y. Sun, F. Dong, Photo-switchable oxygen vacancy as the dynamic active site in the photocatalytic NO oxidation reaction, *ACS Catal.* 12 (2022) 14015–14025.
- [44] J. Yu, J. González-Cobos, F. Dappozze, F.J. López-Tenllado, J. Hidalgo-Carrillo, A. Marinas, P. Vernoux, A. Caravaca, C. Guillard, WO₃-based materials for photoelectrocatalytic glycerol upgrading into glyceraldehyde: unravelling the synergistic photo- and electro-catalytic effects, *Appl. Catal. B Environ.* 318 (2022) 121843.
- [45] Y. Yang, C. Chen, X. Wang, Oxygen vacancy luminescence and band gap narrowing driven by Ce ion doping with variable valence in SnO₂ nanocrystals, *Ceram. Int.* 49 (2023) 24922–24930.
- [46] J. Wang, Z. Wang, B. Huang, Y. Ma, Y. Liu, X. Qin, X. Zhang, Y. Dai, Oxygen vacancy induced band-gap narrowing and enhanced visible light photocatalytic activity of ZnO, *ACS Appl. Mater. Inter.* 4 (2012) 4024–4030.
- [47] H. Wu, Z. Hu, R. Liang, O.V. Nkwachukwu, O.A. Arotiba, M. Zhou, Novel Bi₂Sn₂O₇ quantum dots/TiO₂ nanotube arrays S-scheme heterojunction for enhanced photoelectrocatalytic degradation of sulfamethazine, *Appl. Catal. B Environ.* 321 (2023) 122053.
- [48] R. Liang, Z. Hu, H. Wu, S. Li, X. Zhang, O.A. Arotiba, M. Zhou, Ti³⁺ self-doped and nitrogen-annealed TiO₂ nanocone arrays photoanode for efficient visible-LED-light-driven photoelectrocatalytic degradation of sulfamethazine, *Sep. Purif. Technol.* 314 (2023) 123591.
- [49] J. Zhang, G. Zhang, H. Lan, H. Liu, J. Qu, Sustainable nitrogen fixation over Ru single atoms decorated Cu₂O using electrons produced from photoelectrocatalytic organics degradation, *Chem. Eng. J.* 428 (2022) 130373.
- [50] X. Mei, J. Bai, S. Chen, M. Zhou, P. Jiang, C. Zhou, F. Fang, Y. Zhang, J. Li, M. Long, B. Zhou, Efficient SO₂ removal and highly synergistic H₂O₂ production based on a novel dual-function photoelectrocatalytic system, *Environ. Sci. Technol.* 54 (2020) 11515–11525.
- [51] Z. Wang, S. Xu, J. Cai, J. Ma, G. Zhao, Perspective on photoelectrocatalytic removal of refractory organic pollutants in water systems, *ACS EST Engg* 2 (2022) 1001–1014.
- [52] S. Li, M. Zhou, H. Wu, G. Song, J. Jing, N. Meng, W. Wang, High-efficiency degradation of carbamazepine by the synergistic electro-activation and bimetallic (FeCo@NC) catalytic-activation of peroxymonosulfate, *Appl. Catal. B Environ.* 338 (2023) 123064.
- [53] T. Wang, F. Ye, S. Wu, S. Chen, H. Yu, X. Quan, Efficient light-driven fuel cell with simultaneous degradation of pollutants on a TiO₂ photoanode and production of H₂O₂ on a gas diffusion electrode cathode, *ACS EST Engg* 1 (2021) 1122–1130.
- [54] W. Tian, C. Chen, L. Meng, W. Xu, F. Cao, L. Li, PVP treatment induced gradient oxygen doping in In₂S₃ nanosheet to boost solar water oxidation of WO₃ nanoarray photoanode, *Adv. Energy Mater.* 10 (2020) 1903951.
- [55] K. Song, H. Hou, D. Zhang, F. He, W. Yang, In-situ cation-exchange strategy for engineering single-atomic Co on TiO₂ photoanode toward efficient and durable solar water splitting, *Appl. Catal. B Environ.* 330 (2023) 122630.
- [56] X. Liu, H. Zhou, S. Pei, S. Xie, S. You, Oxygen-deficient WO_{3-x} nanoplate array film photoanode for efficient photoelectrocatalytic water decontamination, *Chem. Eng. J.* 381 (2020) 122740.
- [57] Z. Kang, H. Si, S. Zhang, J. Wu, Y. Sun, Q. Liao, Z. Zhang, Y. Zhang, Interface engineering for modulation of charge carrier behavior in ZnO photoelectrochemical water splitting, *Adv. Funct. Mater.* 29 (2019) 1808032.
- [58] Y. Cheng, J. Kang, P. Yan, J. Shen, Z. Chen, X. Zhu, Q. Tan, L. Shen, S. Wang, S. Wang, Surface oxygen vacancies prompted the formation of hydrated hydroxyl groups on ZnO_x in enhancing interfacial catalytic ozonation, *Appl. Catal. B Environ.* 341 (2024) 12325.
- [59] J. Qi, X. Yang, P.-Y. Pan, T. Huang, X. Yang, C.-C. Wang, W. Liu, Interface engineering of Co(OH)₂ nanosheets growing on the KNbO₃ perovskite based on electronic structure modulation for enhanced peroxymonosulfate activation, *Environ. Sci. Technol.* 56 (2022) 5200–5212.
- [60] H. Feng, J. Yu, L. Tang, G. Zeng, W. Tang, J. Wang, T. Luo, B. Peng, B. Song, L. Wang, C. Liang, Tuning electron density endows Fe_{1-x}Co_xP with exceptional capability of electrooxidation of organic pollutants, *Environ. Sci. Technol.* 53 (2019) 13878–13887.
- [61] S. Lu, X. Li, Y. Cheng, J. Zhou, G. Zhang, In situ electrogenerated Cu(III) triggers hydroxyl radical production on the Cu-Sb-SnO₂ electrode for highly efficient water decontamination, *Proc. Natl. Acad. Sci. USA* 120 (2023) e2306835120.
- [62] K. Wang, R. Mao, R. Liu, J. Zhang, H. Zhao, W. Ran, X. Zhao, Intentional corrosion-induced reconstruction of defective NiFe layered double hydroxide boosts electrocatalytic nitrate reduction to ammonia, *Nat. Water* 1 (2023) 1068–1078.
- [63] A. Wang, Y. Chen, Z. Zheng, H. Wang, X. Li, Z. Yang, R. Qiu, K. Yan, In situ N-doped carbon-coated mulberry-like cobalt manganese oxide boosting for visible light driving photocatalytic degradation of pharmaceutical pollutants, *Chem. Eng. J.* 411 (2021) 128497.
- [64] C. Zhang, S. Tian, F. Qin, Y. Yu, D. Huang, A. Duan, C. Zhou, Y. Yang, W. Wang, Y. Zhou, H. Luo, Catalyst-free activation of permanganate under visible light irradiation for sulfamethazine degradation: experiments and theoretical calculation, *Water Res* 194 (2021) 116915.
- [65] Q. Wang, M. Xiao, Z. Peng, C. Zhang, X. Du, Z. Wang, W. Wang, Visible LED photocatalysis combined with ultrafiltration driven by metal-free oxygen-doped graphitic carbon nitride for sulfamethazine degradation, *J. Hazard. Mater.* 439 (2022) 129632.
- [66] Z. Hu, M. Zhou, H.A. Maitlo, R. Liang, Y. Zheng, H. Wu, X. Song, O.A. Arotiba, Novel dual-photoelectrode photoelectrocatalytic system based on TiO₂ nanoneedle arrays photoanode and nitrogen-doped carbon dots/Co₃O₄ photocathode for efficient water purification at low/no applied voltage, *Appl. Catal. B Environ.* 331 (2023) 122676.
- [67] C. Guo, P. He, R. Cui, Q. Shen, N. Yang, G. Zhao, Electrochemical CO₂ reduction using electrons generated from photoelectrocatalytic phenol oxidation, *Adv. Energy Mater.* 9 (2019) 1900364.